

MICROCOPY RESOLUTION TEST CHART  
NATIONAL BUREAU OF STANDARDS-1963-A

ADA130649

AFGL TR-87-0383  
ENVIRONMENTAL RESEARCH PAPER NO. 813



# Diagnosis of the Comma Cloud of 10 April 1979

DANIEL V. RIDGE, Capt, USAF

14 December 1982

Approved for public release; distribution unlimited.

DTIC  
ELECTE  
JUL 7 1983  
S A D

DTIC FILE COPY

METEOROLOGY DIVISION PROJECT 6670  
AIR FORCE GEOPHYSICS LABORATORY  
HANCOM AFB, MASSACHUSETTS 01731

AIR FORCE SYSTEMS COMMAND, USAF



83 07

This report has been reviewed by the ESD Public Affairs Office (PA)  
and is releasable to the National Technical Information Service (NTIS).

This technical report has been reviewed and  
is approved for publication.

  
DR. ALVA T. STAIR, Jr.  
Chief Scientist

Qualified requestors may obtain additional copies from the  
Defense Technical Information Center. All others should apply  
to the National Technical Information Service.



Unclassified

SECURITY CLASSIFICATION OF THIS PAGE(When Data Entered)

20. (Contd)

*cont* → Five mesoscale waves in the mid- to high-troposphere strongly affected the weather patterns on 10 April 1979. These disturbances had wavelengths from 500 to 800 km, phase speeds of 20 to 33 m/s, and 500 mb height amplitudes around 30 m. They showed excellent time continuity in the 500 mb relative vorticity analyses.

Both omega analyses showed 500 mb rising motion in eastern New Mexico six hours before a subsynoptic surface low and tornadic storms developed just to the east in Texas. Kinematic omegas indicated subsidence over the Texas coastal plain for six hours in the afternoon, evidently associated with maintenance of a surface pressure ridge and an intense low-level inversion which inhibited convection in that area.

Because of its ageostrophic sensitivity and computational ease, kinematic omega is more useful than QG omega for operational purposes. However, the two methods make an independent and complementary pair for research purposes. That part of QG omega forced by the advection of vorticity by the thermal wind approximates total QG omega very well, except in small areas evidently associated with intense vorticity maxima in the cold core of the 500 mb low.

Unclassified

SECURITY CLASSIFICATION OF THIS PAGE(When Data Entered)

## Preface

This research was done in connection with graduate study at the University of Oklahoma funded by the Air Force Institute of Technology. Much of the work was accomplished at the Air Force Geophysics Laboratory.

Thanks to Dr. Howard B. Bluestein for his ideas, criticisms, and support from start to finish, and to Drs. Rex Inman and Fred Carr for their help with theoretical details and computational techniques. Don Chisholm made a detailed critique of my master's thesis and encouraged me to write this abridged report. Betty Blanchard typed this report.



Accession For	
1. Title	<input checked="" type="checkbox"/>
2. Author	<input type="checkbox"/>
3. Subject	<input type="checkbox"/>
4. Abstract	
5. Bibliography	
6. Other Notes	
7. Remarks	
8. Date	

A

## Contents

1. INTRODUCTION	7
2. CASE SELECTION AND METHODOLOGY	8
2.1 Case Selection	8
2.2 Data Preparation	9
2.3 Objective Analysis	12
2.4 Vertical Motion Calculations	18
3. DISCUSSION AND RESULTS	22
3.1 Daybreak, 10 April 1979	24
3.2 Mid-morning, 10 April 1979	27
3.3 Noon, 10 April 1979	30
3.4 Early Afternoon, 10 April 1979	33
3.5 Late Afternoon, 10 April 1979	37
3.6 Evening, 10 April 1979	40
3.7 Midnight, 10-11 April 1979	44
3.8 Early Morning, 11 April 1979	47
3.9 Dawn, 11 April 1979	50
3.10 The Traditional Partition of Quasi-geostrophic Omega	50
4. CONCLUSIONS AND RECOMMENDATIONS	56
REFERENCES	59

## Illustrations

1. Computational Grid, SESAME Rawinsonde Stations, and Supplemental Rawinsonde Stations	10
2. Time-averaged 700 mb Height 10-11 April 1979	11
3. Time-averaged 500 mb Height 10-11 April 1979	11
4. Time-averaged 200 mb Height 10-11 April 1979	11
5. Surface, Neph-, 500 mb, and Omega Analyses at 1200 GMT 10 April 1979	25
6. Surface, Neph-, 500 mb, and Omega Analyses at 1500 GMT 10 April 1979	28
7. Surface, Neph-, 500 mb, and Omega Analyses at 1800 GMT 10 April 1979	31
8. Surface, Neph-, 500 mb, and Omega Analyses at 2100 GMT 10 April 1979	35
9. Surface, Neph-, 500 mb, and Omega Analyses at 0000 GMT 11 April 1979	38
10. Surface, Neph-, 500 mb, and Omega Analyses at 0300 GMT 11 April 1979	42
11. Surface, Neph-, 500 mb, and Omega Analyses at 0600 GMT 11 April 1979	45
12. Surface, Neph-, 500 mb, and Omega Analyses at 0900 GMT 11 April 1979	48
13. Surface, Neph-, 500 mb, and Omega Analyses at 1200 GMT 11 April 1979	51
14. Traditional Partition of Quasi-geostrophic Omega for All Nine Analyses	53

## Tables

1. Analysis Strategy	14
2. Standard Deviation of First-pass Analyzed Heights and Wind Speeds of All Data	15
3. Criteria for Error Identification	16
4. Final rms Height and Vector Wind Speed Errors at 500 mb and 200 mb	17
5. Area Averaged Static Stability	21

## Diagnosis of the Comma Cloud of 10 April 1979

### 1. INTRODUCTION

The cloud patterns associated with synoptic scale, midlatitude cyclonic disturbances usually take on a spiral shape equatorward of the upper cyclone with a broader region of cloudiness spreading poleward across the path of the upper trough. Often the pattern is isolated from other cloudy regions, taking the shape of a vast comma ~2000 km long; and by common usage, any vaguely similar cloud pattern that accompanies short waves in the westerlies has come to be known as a "comma cloud."

Unfortunately, the term "comma cloud" is used also to refer to meso- $\alpha$  cloud vortices ~300 km long, which occur with vorticity maxima in the relatively cold air around upper level extratropical cyclones (see Miller and McGinley).<sup>1</sup>

Boucher and Newcomb<sup>2</sup> proposed a model of the lifecycle of the synoptic scale vortex patterns related to the evolving surface frontal waves with which they are associated. Efforts to infer the vertical motion field in the vicinity of comma clouds directly from satellite observed cloudiness failed (Timchalk and Hubert,<sup>3</sup> Leese,<sup>4</sup> Hansen and Thompson,<sup>5</sup> Nagel et al.,<sup>6</sup> Barr et al.<sup>7</sup>), but the work demonstrated that:

(1) Instantaneous vertical velocity fields do not agree with synoptic-scale cloud patterns, except possibly in the early stages of storm development. Maxima of instantaneous upward and downward motion tend to be upstream of the centers of

---

(Received for publication 8 December 1982)

(Due to the large number of references cited above, they will not be listed here. See References, page 59.)

cloudy and cloud-free areas, respectively, especially in rapidly moving systems. This reinforces the view that clouds result from the time-integrated ascent of parcels which often become saturated somewhere downstream of the maximum of instantaneous ascent.

(2) Other factors, such as moisture stratification and the history of vertical motion, which air parcels have experienced, control the development and dissipation of clouds.

(3) The shape of major cloud patterns is due mainly to the horizontal advection of pre-existing cloud matter.

This study will attempt to verify, as did Barr et al<sup>7</sup> that, despite the disregard of ageostrophic advection and other important physical processes, quasi-geostrophic analysis is able to resolve features having a much smaller scale than that appropriate to the theory. It will compare vertical motion fields calculated by the kinematic and quasi-geostrophic methods. Finally, it will test the usefulness of an alternate partition of the quasi-geostrophic forcing function.

The primary purpose of this research was to verify and refine the model of the three-dimensional flow near developing comma clouds (see Carlson<sup>8</sup> and Millard and Carr<sup>9</sup>) on the basis of fine-scale data, so that forecasters may eventually judge more accurately the location and strength of disturbances indicated by this type of characteristic cloud pattern.

## 2. CASE SELECTION AND METHODOLOGY

### 2.1 Case Selection

Inspection of geostationary satellite imagery reveals that in only one case during the 1978 and 1979 Atmospheric Variability Experiment (AVE) did a clearly outlined comma cloud cross a dense rawinsonde network, on 10-11 April 1979. The "regional scale" rawinsonde network captured all of the associated storm at lower levels--the dry southwest quadrant, the moist southeast quadrant, and the cool airmass north of the warm front. In mid- to high-levels, the trough was slightly west of the AVE-SESAME-1 rawinsonde network until 0600 GMT 11 April 1979, but standard upper air data supplemented the analysis every 12 hours.

---

8. Carlson, T.N. (1980) Airflow through midlatitude cyclones and the comma cloud pattern, Mon. Wea. Rev. 108:1498-1509.

9. Millard, J., and Carr, F. (1982) Composite study of comma clouds and their association with severe weather over the great plains, in Preprints of the 9th Conference on Weather Forecasting and Analysis (Seattle), American Meteorological Society, Boston, pp 402-406.

Associated tornadoes, duststorms, and other severe weather occurred in the SESAME network on this day, including the infamous Wichita Falls, Texas, tornado.

Normally, the term "comma cloud" refers to a synoptic-scale cloud shield which evolves rather gradually in a developing extratropical cyclonic disturbance, or to a meso- $\alpha$  scale cloud in the cold core of an upper cyclone. This comma cloud was unusual in that it developed very rapidly from meso- $\alpha$  to macro proportions above an intense squall line (in the middle of the SESAME data set). This case is representative, in the vigorous extreme, of comma clouds which accompany rapid development and changing weather, and a detailed knowledge of its structure is valuable to operational forecasters.

## 2.2 Data Preparation

SESAME rawinsonde data were available on magnetic tape every three hours from 1200 GMT 10 April 1979 to 1200 GMT 11 April 1979, over a "regional scale" network with approximately 214 km average separation of each station from its nearest neighbor. The set contained 335 rawinsonde ascents. Conventional teletype data yielded additional 12-hourly rawinsonde reports and hourly surface observations. Figure 1 illustrates the SESAME stations, the standard rawinsonde stations used, and the analysis grid chosen.

GOES (Geostationary Operational Environmental Satellite) imagery data were used in this study. They consisted of half-hourly satellite photographs with half-mile resolution video data in the daytime and one mile resolution infrared data at night. The National Earth Satellite Service MB enhancement of the gray scale was used for the infrared data. Manually digitized radar data were used to locate convective features when gridding was missing or incorrect on the satellite images. Nephanalyses were prepared by hand from these satellite images and radar charts, focusing on the convective areas, the duststorm, and the thunderstorm cirrus canopy which evolved into a comma cloud.

Terrain heights were derived from two data sources and then smoothed. For gridpoints on or east of 105° W, a U.S. Air Force data set (Carr<sup>10</sup>) at 1° latitude-longitude interval was interpolated linearly, while west of 105° W, heights were estimated from a 1:3 million scale weather chart.

Before rawinsonde information was archived on magnetic tape, it was decoded, checked for errors both manually and by machine, and linearly interpolated

---

10. Carr, F. (1981) Personal communication.



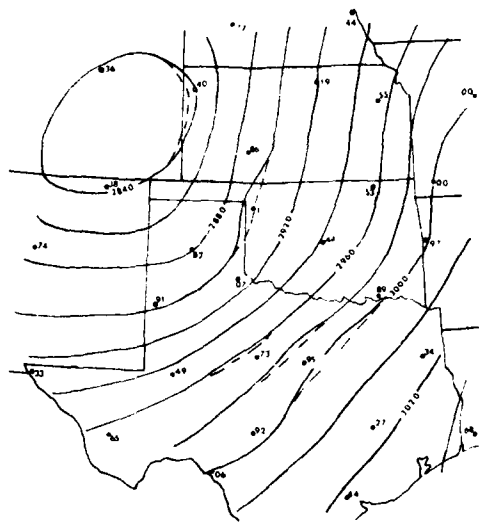


Figure 2. Time-averaged 700 mb Height 10-11 April 1979. Subjective corrections shown as dashed lines

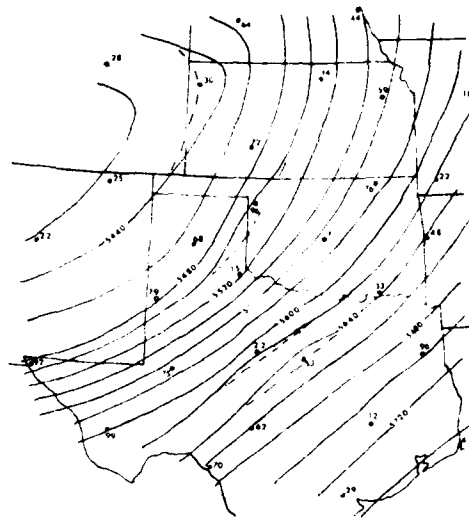


Figure 3. Time-averaged 500 mb Height 10-11 April 1979. Subjective corrections shown as dashed lines

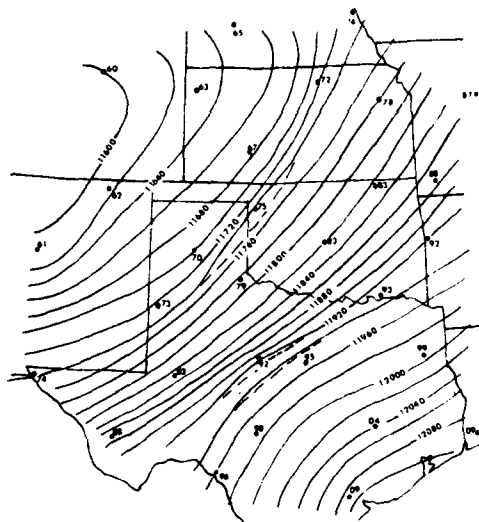


Figure 4. Time-averaged 200 mb Height 10-11 April 1979. Subjective corrections shown as dashed lines

obtained for each station. These were used to prepare time-averaged constant-pressure height charts for 700 mb, 500 mb, and 200 mb. The average-height charts were analyzed manually at a 20-m interval and are shown as Figures 2-4. From these fields it was determined that several stations had height errors persistent in time and pressure level. Although other interpretations of Figures 2-4 may be possible, we felt that a desired result of any data adjustment should be to weaken the height gradients and curvature of contours which in the original data appeared to be too intense. This was done by adjusting downward the heights of all rawinsonde reports for three stations [Gage, Oklahoma (17 m high); Abilene, Texas (12 m high); and Stephenville, Texas (7 m high)], and by adjusting upward the heights of a fourth station [Goodland, Kansas (5 m low)], before using the rawinsonde data in the objective analysis. The identification and correction of individual errors is explained in Section 2.3.

The SESAME data sets include the balloon release time and location of the balloon relative to the tracking station during ascent. Based on results of earlier studies<sup>14, 15</sup> observations were inserted into analyses at the actual balloon location downwind of the rawinsonde station at each pressure level, rather than at the station location. All data were linearly interpolated or extrapolated to a common balloon release time one hour before the nominal data time. For example, data interpolated to a 1400 GMT release were labeled "1500 GMT rawinsonde".

Because of the location of the cloud vortex on the western edge of the SESAME network, the analyses were augmented with standard 12-hourly rawinsonde data from stations near the western part of the grid (see Figure 1). However, only the analyses at 1200 GMT 10 April 1979, and 0000 and 1200 GMT 11 April 1979 had the benefit of this extra information, while the analyses at 1500, 1800, 2100, 0300, 0600, and 0900 GMT did not.

Height, wind direction, and wind speed for these 12-hourly rawinsondes were extracted from standard teletype data for mandatory levels and interpolated logarithmically to non-mandatory levels (1000, 900, 800, and 600 mb).

14. Moore, J., and Fuelberg, H. E. (1981) A synoptic analysis of the first AVE-SESAME '79 period, Bull. Am. Meteor. Soc. 62:1577-1590.
15. Jedlovec, G., and Fuelberg, H. E. (1981) A synoptic-scale kinematic energy analysis of the 10-11 April SESAME '79 period, in Proceedings of the SESAME 1979 Preliminary Results Workshop, Huntsville, Alabama, pp 2-123.

### 2.3 Objective Analysis

Cressman's<sup>16</sup> successive approximation procedure for interpolating values of randomly spaced data to regularly spaced gridpoints was used in this study. Data within a fixed horizontal "radius of influence",  $R$ , of a given gridpoint were averaged after weighting by the Cressman weighting function,  $w$ :

$$S_o = \frac{\sum_{i=1}^n (w_i S_i)}{\sum_{i=1}^n w_i}, \quad (1)$$

for

$$w_i = \frac{R^2 - d_i^2}{R^2 + d_i^2} \quad (2)$$

where data,  $S_i$ , observed at locations  $(x_i, y_i)$  within the radius of influence,  $R$ , of the gridpoint  $(x_o, y_o)$  were weighted relative to the distance  $d_i$ . Each pressure level was considered independent of data above or below the level. If rawinsonde reports of height and wind were both available, the height estimate,  $z_i$ , was augmented by the height gradient computed from the observed wind, and the compound report was weighted four times a simple height report (Cressman<sup>16</sup>).

This procedure is sensitive to many factors which can affect the quality of the analysis, such as the choice of the rectangular grid spacing,  $d$ , and the maximum radius,  $R$ , at which data points influence a gridpoint. An overview of the problems involved will make the solutions taken in this research more understandable.

Given data separated in the average by  $s = 214$  km, one would like to define gridded values at an interval much smaller than  $s$ . However, the expected variance of interpolation error (for the best analysis conditions) increases rapidly<sup>17</sup> as the grid distance decreases below  $s$ . Since the choice of a grid interval only slightly less than  $s$  ( $d = s/1.33$ ) reduces this problem,  $d$  was set to 161 km. In addition, interpolation error is sensitive to the range of radii of influence,  $R$ , used in the Cressman analysis. In order to minimize the error generated by the interpolation in Eq. (1), one must apply a strategy of using successively smaller  $R$  with increasingly more restrictive error identification within a range of radii identified by Stephens and Stitt.<sup>17</sup> They advise a lower limit on  $R$  of approximately  $1.5d$ . The determination of an upper bound on  $R$  was important because of the absence of an acceptable first-guess field for the analysis. Because of the strong gradients

16. Cressman, G. P. (1959) An operational objective analysis system, Mon. Wea. Rev. 87:367-374.

17. Stephens, J. J., and Stitt, J. M. (1970) Optimum influence radii for interpolation with the method of successive corrections, Mon. Wea. Rev. 98:680-687.

and dynamic nature of the weather situation, a constant-value first guess was deemed inappropriate. Therefore, an examination of analysis sensitivity to R was made with values of R from 1.5d to 3.5d. This study indicated that this SESAME data set yields a reasonably smooth height analysis for  $R \geq 3d$ , which became the radius of influence for the analysis first-pass (that is, the first-guess) for each of the nine 3-hourly data sets.

Table 1 shows the five steps which were applied in the objective analysis phase of this study, with R ranging from 3d down to 2d. Pass I created a first guess field from the reported data, without reference to data at any other pressure level or time. Every field except the last pass was smoothed with a simple smoothing operator to eliminate high frequency noise. Note also that the Cressman weighting function filters much noise at wavelengths less than 2R (Stephens<sup>18</sup>). No analysis, objective or subjective, can extract real, unambiguous information about disturbances of wavelength less than 2s, where s is the average station separation of the SESAME data set. Therefore, for the last pass, when  $2R = 3s$ , noise at wavelengths less than 2s was definitely eliminated by the Cressman analysis without need for final smoothing. Since the individual observations may contain unacceptable errors, a pass-by-pass procedure of error checking was used. The Pass I field was used only to identify the most erroneous data (by a method which will be discussed below). After Passes II, III, and IV, the latest values of all fields were substituted for missing reports in the original data set and used as bogus data for the next pass.

Table 1. Analysis Strategy

Pass I	R = 3.00d = 483 km Check errors, but do not bogus.	Smooth.
Pass II	R = 3.00d = 483 km Check errors and bogus missing data.	Smooth.
Pass III	R = 2.67d = 429 km Check errors and bogus.	Smooth.
Pass IV	R = 2.33d = 367 km Check errors and bogus.	Smooth
Pass V	R = 2.00d = 322 km	Do not smooth.

18. Stephens, J. J. (1967) Filtering response of selected distance-dependent weight functions, Mon. Wea. Rev. 95:45-46.

The analysis region has  $11 \times 12$  points on a polar stereographic projection in the horizon and eleven levels in the vertical: the surface plus every 100 mb from 1000 mb to 100 mb. Gridpoints below the smooth terrain analysis were flagged immediately after the height analysis for each data set. The pressure-coordinate scheme was chosen for this study because it is simpler than a terrain following  $\sigma$ -coordinate system, given that the data were supplied at constant pressure levels. The  $\sigma$ -coordinate system would require interpolation of data from pressure to  $\sigma$ -coordinates for computation then back to pressure coordinates for graphic display. It was hoped that vertical finite differencing over intervals of constant pressure would yield more consistent results than differencing over  $\sigma$ -coordinate intervals, which vary in pressure separation. For these reasons, the pressure coordinate system was chosen.

After each analysis pass, all data were checked against an analyzed value at the rawinsonde location, calculated by bilinear interpolation of the latest gridded analysis. Each deviation was checked against an error criterion which varied with pressure level, with parameter, and with the radius of influence,  $R$ . If the deviation was less than the criterion, the observed value was stored in a working rawinsonde array. Otherwise, the observation was disregarded for that particular pass, and the analyzed value was stored as a bogus observation in the working array. This working rawinsonde array was used as input to the next pass analysis. The original reports, including missing flags, were stored for reference throughout the analysis, and re-checked against later pass analyses. Thus, observations considered "bad" relative to an early, rough analysis could be used later when their comparison to more consistent analyses indicated the observation was "good".

A visual inspection of the observation/analysis deviations of height and vector wind for some of the data showed that the statistical properties of the data set itself should dictate the height and wind error criteria. Each of the nine data sets was analyzed by a single pass with  $R=3d$ , giving nine separate analyzes of  $z$ ,  $u$ , and  $v$  at each level, and the root-mean-squares (rms) of all data at each pressure level were accumulated and are illustrated in Table 2.

Table 2. Standard Deviations of First-pass Analyzed Heights and Wind Speeds Accumulated From All Nine Sets of Observed Data

p (mb)	sfc	1000	900	800	700	600	500	400	300	200	100
$\sigma_z$ (m)	-	8.5	14.8	16.9	15.1	18.8	19.6	22.6	28.5	30.5	24.7
$\sigma_v$ (m/s)	4.8	3.6	5.4	6.6	6.5	7.3	8.8	9.8	11.3	9.2	6.5

These standard deviations were used to define basic height-dependent criteria,  $\delta_z$  and  $\delta_v$ , for testing errors in height and wind, respectively. The basic criterion  $\delta_T$  for temperature was taken as twice the rms error of rawinsonde sensors expected for AVE data<sup>11</sup> and was applied independent of height. For the surface pressure tendency,  $\delta_\chi$  is taken as 50 percent in order to eliminate only the worst errors.

In order to restrict the error tolerances more and more with each analysis pass, the criteria for error identification were decreased linearly in R from  $2\delta_\pi(p)$  at  $R=3d$ , to  $\delta_\pi(p)$  at  $R=2d$ , where  $\delta_\pi(p)$  is one of the basic pressure-dependent criteria relative to the parameters ( $\pi$ ) which were analyzed. Table 3 indicates the numerical definition of the basic criteria and the testing inequalities which were applied to each piece of data after each analysis pass. Subscripts o and a refer to observed data and analyzed values of height, u and v wind components pressure tendency, temperature and relative humidity;  $\sigma_z$  and  $\sigma_v$  are the pressure-dependent standard deviations of height and wind speed for the entire SESAME data set which are listed in Table 2. The factor (R-1) decreases the criteria linearly with R, the radius of influence.

Table 3. Criteria ( $\delta_z$ ,  $\delta_v$ ,  $\delta_\chi$ ,  $\delta_T$ ) for Error Identification. The variables  $\pi$  are: height (z), vector wind ( $\vec{V}$ ), surface pressure tendency ( $\chi$ ), and temperature (T). See text for explanation

$\pi$ :	Basic Criterion:	Application:
Z	$\delta_z = \sigma_z(p)$ (m)	$ Z_o - Z_a  \geq (R-1) \delta_z$
$\vec{V}$	$\delta_v = \sigma_v(p)$ (m/sec)	$ (u_o - u_a)^2 + (v_o - v_a)^2 ^{1/2} \geq (R-1) \delta_v$
$\chi$	$\delta_\chi = 50\%$	$ (\chi_o - \chi_a)/\chi_o  \geq (R-1) \delta_\chi$ or $(\chi_o \chi_a) < 0$
T	$\delta_T = 2^\circ\text{C}$	$ T_o - T_a  \geq (R-1) \delta_T$

Table 4 shows the rms deviations of analyzed fields from the observed data after five analysis passes at 500 and 200 mb for the nine analysis times studied. For this purpose the original observations, including those rejected by the error-identification scheme, have been used to determine residual errors. Errors at other levels are tabulated in Ridge.<sup>19</sup>

19. Ridge, D. (1982) Diagnosis of the Comma Cloud of 10 April 1979, Master's thesis, University of Oklahoma, Norman, Oklahoma, 108 pp.

Table 4. Final rms Height and Vector Wind Speed Errors for Each Data Set at 500 mb and 200 mb

Time (GMT)	z(m)   $\vec{V}$   (m/sec)		z(m)   $\vec{V}$   (m/sec)	
	(500 mb)		(200 mb)	
1200	5.5	3.1	9.6	5.3
1500	6.6	3.2	9.8	6.3
1800	5.5	3.4	12.1	4.5
2100	6.5	5.0	39.8	5.3
0000	8.8	4.9	23.8	3.8
0300	6.9	4.8	23.1	4.8
0600	6.4	8.2	16.6	9.1
0900	10.0	6.4	14.0	13.2
1200	11.4	4.0	10.5	6.5
	( $\delta_z = 19.6$ )	( $8.8 = \delta_v$ )	( $\delta_z = 30.5$ )	( $9.2 = \delta_v$ )

Some of the values at 200 mb are larger than the criteria  $\delta_z$  and  $\delta_v$ , and they deserve the following explanation.

At 2100 GMT,  $\sigma_z(200 \text{ mb}) = 18.6 \text{ m}$  for 31 stations inside the analysis grid. However, one station (COU) with a 200 m indicated error raises the  $\delta_z$  for all 32 stations to 39.8 m. The analyzed height at COU is consistent in time and space with all data, except the 2100 GMT sounding at COU. The COU heights are reasonable as high as 500 mb, but the indicated error increases from 38 m at 400 mb, to 115 m at 300 mb, to 200 m at 200 mb; and they lose consistency with the 1800 and 0000 GMT soundings from COU. Temperature reports are exceedingly warm in this part of the sounding. All the evidence indicates that the 2100 GMT rawinsonde from COU failed above 500 mb, that the reported heights were bad, and that the analysis scheme was able to identify the error.

At 0900 GMT,  $\sigma_v(200 \text{ mb}) = 13.2$ , mainly because the analysis smoothed a very strong jet maximum. The strongest wind at 200 mb at that time was at OKC, reported at 83 m/sec but analyzed as 41 m/sec, with a 43 m/sec vector deviation from the observation.

A thorough search for the causes of large rms errors indicated that the height analysis dealt with height errors very well, but that the wind analysis smoothed jet streaks to half the intensity shown in a subjective analysis and also removed mesoscale troughs evident in subjectively-drawn 500 mb streamline analyses. From the understatement of horizontal wind gradients in such regions, one must expect weaker values of kinematically computed vertical motion than a better wind analysis might reveal. However, the results of this kinematic analysis (see Section 3) compare very well qualitatively to an analysis of kinematic omega in this SESAME data set by Moore and Fuelberg.<sup>14</sup>

#### 2.4 Vertical Motion Calculations

Two methods of calculating vertical motion were used in this study, namely the kinematic and the quasi-geostrophic (QG) methods. The QG omega equation was chosen for two reasons. First, the calculation of vertical motion may be separated into two physically meaningful parts.<sup>20</sup> The QG analysis is a compromise between the kinematic method, a straightforward method which provides no such physical insight, and more complicated forms of the omega equation which also account for latent heat release, surface friction, advection by the ageostrophic part of the wind, and so on. Second, these calculations, based entirely on a smooth height analysis, eliminate a large cumulative error characteristic of the kinematic method which can result from minor noise in the wind field. Both of these points present paradoxes, however, which underscore the independence of the two methods. Krishnamurti<sup>21</sup> demonstrated what operational forecasters have long known, that the two physically meaningful parts of QC forcing do not always adequately define the total response of the atmosphere to complex forcing. Using only the first two terms, one must rely on experience and empirical guidance to decide whether the ageostrophic forces may dominate in some area, and what changes they will cause in the height field. Second, the kinematic method (adjusted) often yields omega fields which compare well to the observed clouds and weather despite the potential problem of noise. Again, the analyst can never be certain whether any particular kinematic analysis is better or worse than the corresponding QG analysis without comparing the fields to cloud, precipitation, or moisture patterns, or by calculating some higher order version of the omega equation.<sup>21</sup>

With the QG omega equation, vertical motion was computed over a  $7 \times 8$  grid-point interior domain ( $\omega = 0$  around the sides) using boundary conditions specified at 100 mb ( $\omega = 0$ ) and at the first vertical level above terrain (generally 800 mb in the west and 900 mb in the east of the analysis area in Figure 1). A solution for omega at 100 mb by the adiabatic method was tested as an upper boundary condition in the QG equation but was found to have very little effect on the interior values of QG omega. Kinematic omega was computed over a  $9 \times 10$  grid and adjusted to zero at 100 mb using O'Brien's quadratic technique.<sup>22</sup> All these methods are explained in detail below.

20. Bluestein, H. B. (1979) Quasigeostrophic Theory, unpublished, mimeograph class notes, 52 pp.
21. Krishnamurti, T. N. (1968) A study of a developing wave cyclone, Mon. Wea. Rev. 96:208-217.
22. O'Brien, J. J. (1969) Alternative solutions to the classical vertical velocity problem, J. Appl. Meteor. 9:197-203.

Two types of lower boundary conditions were used, one for each method. First, the kinematic method requires a surface vertical motion which results from observed wind and surface pressure tendency:

$$\omega_s = -\rho_s g(\vec{V}_s \cdot \nabla h) + \chi_s \quad (3)$$

where  $\rho_s$ ,  $\vec{V}_s$ , and  $\chi_s$  are the density, observed wind, and local pressure tendency at the surface,  $h$  is the terrain height, and  $g$  is the acceleration of gravity. Surface pressure, density, and geostrophic wind were computed indirectly based on the hypsometric equation. The observed wind  $\vec{V}_s$  was analyzed objectively from rawinsonde  $u$  and  $v$  components, without the use of hourly surface reports.

The lower boundary condition used for the GQ omega equation was:

$$\omega_g = -\{\rho_s g(\vec{V}_g \cdot \nabla h)\} \quad (4)$$

where

$$\vec{V}_g = \frac{1}{2} \vec{k} \times \frac{1}{\rho_s f_o} \nabla P \quad (5)$$

Here, the surface geostrophic wind,  $\vec{V}_g$ , is taken as half the value indicated by the gradient of pressure,  $P$ , at the terrain height of each gridpoint, in order to account for the decrease in wind speed toward the surface because of friction.<sup>10</sup>

The kinematic method for calculating omega consists of integrating the continuity equation from the surface upward through:

$$\omega_N = \omega_o + \sum_{k=1}^N (p_{k-1} - p_k) \frac{1}{2} (\delta_{k-1} + \delta_k) \quad (6)$$

The average divergence,  $\frac{1}{2} (\delta_{k-1} + \delta_k)$ , over a pressure layer,  $p_{k-1}$  to  $p_k$ , determines the vertical change in omega over the layer. Only a lower boundary value,  $\omega_o$ , is required to initiate the integration.

If one assumes wind errors at neighboring gridpoints to be independent of one another, then the horizontal gradient of wind would have an rms error of  $\sigma_v/d$ , because the winds at either end of the  $2d$  interval would each contribute  $\sigma_v$  error. This leads one to expect errors of about  $10 \mu\text{b/s}$  in omega at 100 mb after vertical integration. Before adjustment the rms value of omega at 100 mb calculated by the kinematic method was slightly smaller than this expectation ( $\sim 7.5 \mu\text{b/s}$ ).

A simple but effective technique for adjusting the solution of the kinematic Eq. (6) to some reasonable top boundary value is that due to O'Brien.<sup>22</sup> Suppose

the top value,  $\omega_K$ , of a column of  $K+1$  calculated values of omega is in error by an amount  $(\omega_K - \omega_{top})$  from the desired boundary value,  $\omega_{top}$ . One can distribute a correction to each  $\omega_k$ , either linearly with height:

$$\omega_k' = \omega_k - \frac{k}{K} (\omega_K - \omega_{top}) \quad k=0, K \quad (7)$$

or quadratically:

$$\omega_k' = \omega_k - \frac{k(k+1)}{K(K+1)} (\omega_K - \omega_{top}) \quad k=0, K. \quad (8)$$

The quadratic adjustment [Eq. (8)] makes more adjustment at high levels than at middle levels, makes almost none at low levels, and controls the tendency of the linear operator [Eq. (7)] to spread noise from high-level wind errors downward.

In summary, the final product of O'Brien's quadratic technique in this research conforms very well to the synoptic pattern, suggesting that the actual noise problem is less severe than one might expect from the theory of the kinematic method.

In three dimensions, the QG omega equation is:

$$\nabla^2 \omega + f_0^2 / \sigma \frac{\partial^2 \omega}{\partial p^2} = F(x, y, p) \quad (9)$$

where  $f_0$  is a constant value of the coriolis parameter,  $F(x, y, p)$  is a forcing function, and static stability,  $\sigma$ , depends only on time and pressure. The vertical derivative was computed using finite differences over 200 mb.

The static stability parameter was calculated at each station at each time, every 100 mb from 1000 mb to 100 mb, with the following equation:

$$\sigma = \frac{287 \times T \times \{ \ln(\theta_2) - \ln(\theta_1) \}}{p \times 50 \text{ mb}} \quad (10)$$

where  $T$  is the observed temperature at pressure level  $p$ , and  $\theta_2$  and  $\theta_1$  are the potential temperatures 25 mb respectively above and below pressure level  $p$ . The area averaged sigma is shown in Table 5 as a function of time and pressure. The stability parameters for the NACA Standard Atmosphere were computed from data at 25 mb above and below each pressure level of interest. The strength of the relative maximum of stability at 900 mb is also worthy of note.

Table 5. Area Averaged Static Stability Parameter  $\sigma$  in Units of  $(m^{-1} kg)$  per 100 mb for NACA Standard and for Every Three-hourly SESAME Data Set

p(mb)	Time (GMT)									
	NACA	1200	1500	1800	2100	0000	0300	0600	0900	1200
100	1.830	1.605	1.619	1.586	1.628	1.617	1.633	1.720	1.645	1.639
200	0.450	0.348	0.384	0.392	0.378	0.362	0.348	0.343	0.318	0.320
300	0.070	0.060	0.061	0.070	0.062	0.061	0.058	0.057	0.059	0.077
400	0.042	0.023	0.023	0.022	0.025	0.026	0.022	0.026	0.026	0.027
500	0.027	0.021	0.023	0.019	0.019	0.021	0.017	0.019	0.019	0.019
600	0.020	0.017	0.016	0.017	0.016	0.013	0.013	0.013	0.014	0.016
700	0.015	0.017	0.014	0.016	0.017	0.016	0.014	0.014	0.017	0.014
800	0.012	0.021	0.021	0.017	0.019	0.017	0.017	0.019	0.019	0.018
900	0.010	0.035	0.037	0.035	0.021	0.021	0.024	0.025	0.021	0.023

One object of this study was to compare the difference in physical insights which can be given by two different mathematical partitions of the QG forcing function,  $F(x, y, p)$ . The two partitions of interest are the traditional:

$$F = \frac{f_0}{\sigma} \frac{\partial}{\partial(-p)} (\vec{V}_g \cdot \nabla(\zeta+f)) + \frac{R_d}{\sigma p} \nabla^2 (-\vec{V}_g \cdot \nabla T)$$

$$= F1 + F2 \quad (11)$$

and the alternative

$$F = \frac{f_0}{\sigma} (-\vec{V}_T \cdot \nabla(2\zeta+f)) - \frac{f_0}{\sigma} (E \frac{\partial D}{\partial p} - D \frac{\partial E}{\partial p})$$

$$= F3 + F4 \quad (12)$$

The first term in Eq. (11),  $F1$ , represents forcing by the differential advection of absolute vorticity  $(\zeta+f)$  by the geostrophic wind  $\vec{V}_g$ . The second term,  $F2$ , is forcing by the laplacian of thermal advection by  $\vec{V}_g$ . The alternative partition due to Wiin-Nielsen<sup>23, 24</sup> involves the term  $F3 = (2A+C)$  for the advection of the quantity  $(2\zeta+f)$  by the thermal wind,  $\vec{V}_T$ , and Wiin-Nielsen's  $F4 = (-2 \Lambda)$  deformation function, where  $D$  and  $E$  are given by:

23. Wiin-Nielsen, A. (1959) On a graphical method for an approximate determination of the vertical velocity in the mid-troposphere, Tellus, 11:432-440.
24. Trenberth, K. E. (1977) On the interpretation of the diagnostic quasi-geostrophic omega equation, Mon. Wea. Rev. 106:131-137.

$$D = \frac{\partial v}{\partial x} + \frac{\partial u}{\partial y}; E = \frac{\partial u}{\partial x} - \frac{\partial v}{\partial y}. \quad (13)$$

These are the so-called shearing and stretching parts of deformation.

Wiin-Nielsen's formulation permits an easy visualization of the QG vertical motion from an isobaric chart of temperature and  $(2\zeta+f)$ , providing the F4 forcing function is negligible compared to F3. Using the thermal wind indicated by the direction and spacing of isotherms, the degree of cyclonic vorticity advection is inversely proportional to omega, without the troublesome  $\frac{\partial}{\partial(-p)}$  and  $\nabla^2$  operators in the F1 and F2 terms. One of the secondary objectives of this research is to examine the magnitude of F4 and the resulting portion of QG omega using fine-scale data, in order to verify the utility of this analysis tool in the vicinity of a strong developing wave.

### 3. DISCUSSION AND RESULTS

A few words of explanation will facilitate the discussion of the nine individual, three-hourly data sets. The clouds and weather on 10 April 1979 were influenced very strongly by five meso- $\alpha$  short waves that passed through the area. Meso- $\alpha$  is used here in the context suggested by Orlanski.<sup>25</sup> These disturbances had wavelengths from 500 to 800 km, phase speeds of 20 to 33 m/sec, and amplitudes of around 30 m in the 500 mb height field. They can be followed best in the 500 mb relative vorticity analyses whose magnitude varied  $\pm 5 \times 10^{-5} \text{ sec}^{-1}$  as the minor troughs and ridges passed. Waves of this scale in the extratropical westerlies have not received much attention in the literature. Because these short waves are smaller than the better understood synoptic scale short waves<sup>26</sup> they will be called "minor short waves" or "minor waves" herein. Other researchers have found evidence of these disturbances in this case. They showed up in the 300 mb isotach analyses by Moore and Fuelberg<sup>14</sup> and in the time cross-sections of weather, humidity, and vertical motion by Wilson.<sup>27</sup>

25. Orlanski, I. (1975) A rational subdivision of scales for atmospheric processes. Bull. Am. Meteor. Soc. 56:527-530.

26. Palmen, E., and Newton, C.W. (1969) Atmospheric Circulation Systems, Academic Press, New York, 603 pp.

27. Wilson, G. (1981) Structure and dynamics of important mesoscale systems influencing the thunderstorm development during April 10-11, 1979 (AVE SESAME D), in Proceedings of the SESAME 1979 Preliminary Results Workshop, Huntsville, Alabama, pp 28-31.

In this study, 500 mb ascent downwind of subsidence will be taken as evidence of a minor wave in the mid- to upper-troposphere which should be corroborated in the height and vorticity fields. Each use of the term "500 mb jet" in this discussion will refer to the zone of maximum winds implied by a region of strong 500 mb height contour gradient (see Figures 5c, 6c, 7c, and so on). For brevity, the total quasi-geostrophic omega resulting from the sum of F1 and F2 forcing, will be called QG omega in contrast to the four partitions of this field by differential vorticity advection (F1 omega), Laplacian of thermal advection (F2 omega), advection of vorticity by the thermal wind (F3 omega), and Wiin-Nielsen's deformation function (F4 omega). "Kinematic omega" refers to omega computed kinematically and adjusted by O'Brien's quadratic method. Omega of magnitude greater than  $10 \mu\text{b/s}$  is defined as "strong" vertical motion.

Bear in mind these rawinsonde data sets are just three hours apart over the 24-hour period. Features in the omega analyses which exhibit time continuity should be considered true expressions of the atmosphere while features which appear and disappear within six to nine hours must be judged as noise.

References to tornado and hail occurrences are taken from the damage summaries in Alberty et al.<sup>28</sup>

---

28. Alberty, R.L., Burgess, D.W., Hane, C.E., and Weaver, J.F. (1979) SESAME 1979 Operations Summary, National Oceanic and Atmospheric Administration, Boulder, Colorado, 352 pp.

### 3.1 Daybreak, 10 April 1979

At 1200 GMT (Figures 5a and 5b) showers accompany a low in the lee of the Colorado Rockies, a cold front in New Mexico, and a developing warm front of the Texas coast. Gulf stratus extends up the Rio Grande valley. A 500 mb trough in Kansas (Figure 5c) is minor wave No. 1 of this case study. A 500 mb ridge across the Texas panhandle separates this trough from minor wave No. 2 in New Mexico.

Both the QG and kinematic omega fields (Figures 5d and 5e) show ascent in western Kansas and subsidence in Oklahoma associated with minor wave No. 1. The ascent in this case is not directly downstream from the descent but is located in the cold air on the left of the 500 mb jet which flows from south to north across Kansas (see Figure 5c). Kinematic omega shows 500 mb ascent in the showery region of the Texas coast, while QG omega does not. Both methods show an area of ascent in Eastern New Mexico at least six hours before the appearance of a subsynoptic surface low (SSL) in west Texas (see Figure 8a).

The two methods disagree about the situation over extreme west Texas. Kinematic omega (Figure 5e) suggests rising motion in advance of another minor wave, and kinematic omega three hours later (Figure 6e) reinforces this inference, as weak subsidence appears south of El Paso, Texas. QG omega shows moderate subsidence ( $+7 \mu\text{b/s}$  in Figure 5d) over southern New Mexico. Surface temperatures at Carlsbad and Roswell, New Mexico, rose  $14^\circ\text{C}$  in two hours, suggesting warming by strong subsidence. The dry line probably began moving some time in the next three hours, but it cannot be located well until 1500 GMT (Figure 6a) in southeastern New Mexico. The surface warming supports the QG omega analysis of subsidence behind minor wave No. 2. In West Texas and southern New Mexico, cold advection is balancing subsidence warming, so that 500 mb temperatures are nearly constant (Figures 5c and 6c). Although one might expect the subsidence warming to weaken faster than the horizontal advection cooling well below 500 mb (because the ground does not interrupt horizontal motion as directly as vertical), with consequent low level cooling, the opposite occurs. That is, surface temperatures are rising at the rate of  $14^\circ\text{C}$  in two hours.

Figures 5f and 5d show that F3 omega approximates QG omega very well, but exaggerates the maximum value by 25 percent. Some slight differences may be noted between the QG omega fields (Figures 5d, 6d, and so on), which were computed from the sum of F1 and F2 forcing functions, and the sums of F3 and F4 omega fields (Figures 5f/5g, 6f/6g, and so on). These inconsequential differences are due to minor inconsistencies among the finite-difference representations of derivatives in the F1, F2, F3, and F4 forcing functions (see Ridge).<sup>19</sup>

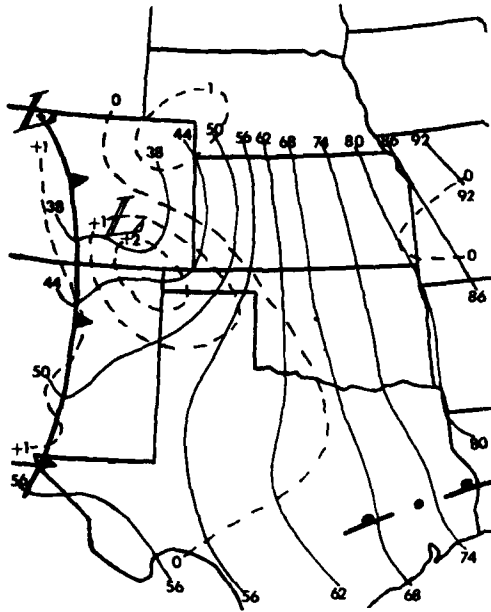


Figure 5a. Surface Fronts and Alt. Setting ( $10^2$  in Hg; solid) and Quasi-geostrophic Surface Omega ( $\mu\text{b/s}$ ; dashed) at 1200 GMT 10 April 1979.

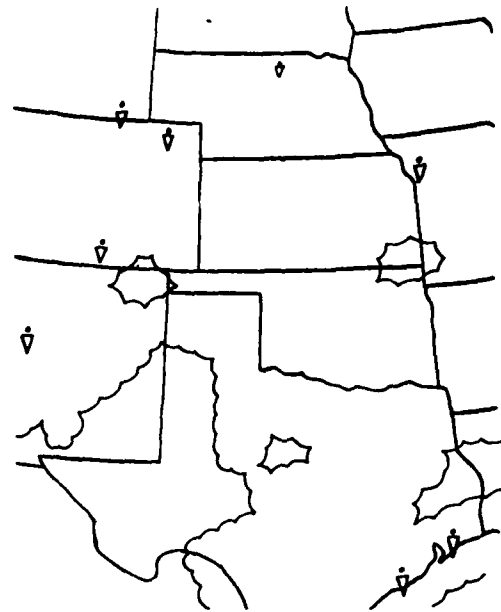


Figure 5b. Nephanalysis at 1200 GMT 10 April 1979 From GOES IR Data, With Convective and Duststorm Activity From Radar and Hourlies. Ceilings inside scallop

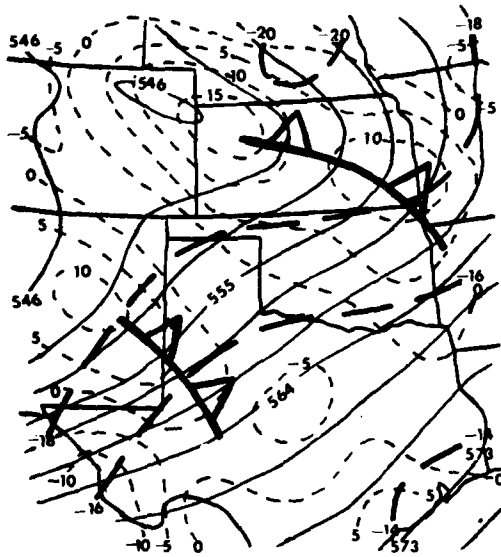


Figure 5c. 500 mb Height (m; solid lines), Temperature ( $^{\circ}\text{C}$ ; heavy dashed), and Relative Vorticity ( $10^{-5} \text{ s}^{-1}$ ; light dashed) at 1200 GMT. Minor wave trough (A)

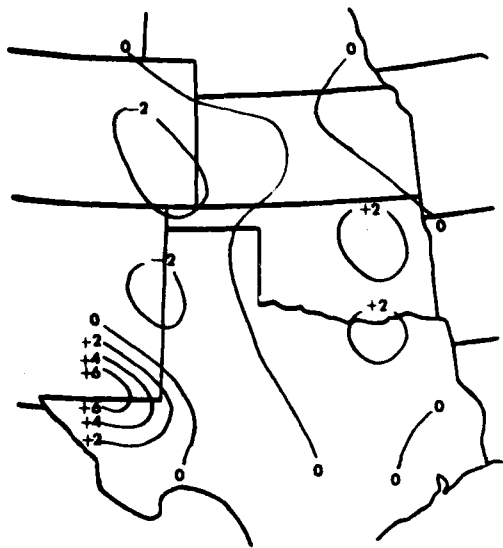


Figure 5d. 500 mb Quasi-geostrophic Omega ( $\mu\text{b/s}$ ) at 1200 GMT 10 April 1979

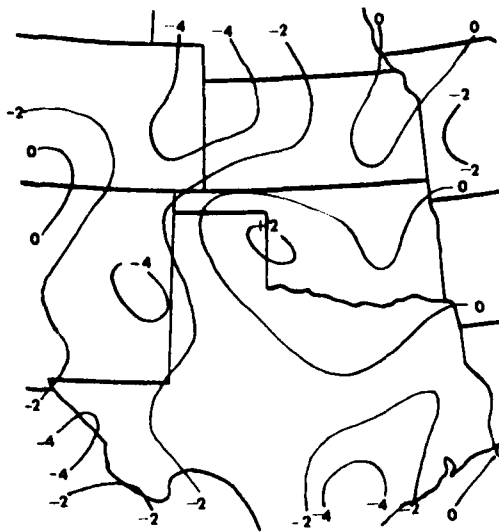


Figure 5e. 500 mb Kinematically Computed Omega ( $\mu\text{b/s}$ ) Corrected by O'Brien's Method, at 1200 GMT 10 April 1979

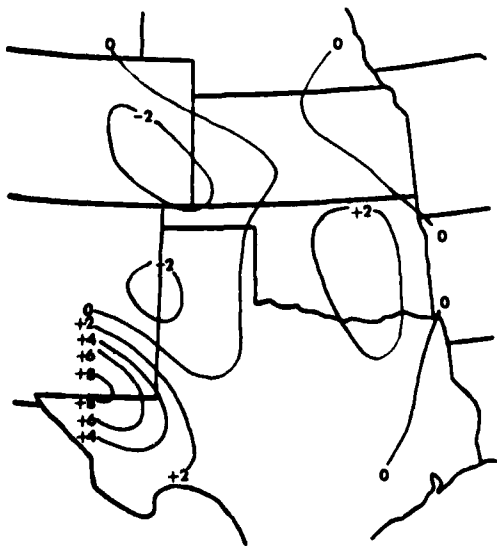


Figure 5f. 500 mb Omega ( $\mu\text{b/s}$ ) Due to the Advection of Vorticity ( $2\zeta + f$ ) by the Thermal Wind ( $F3$ ), at 1200 GMT 10 April 1979

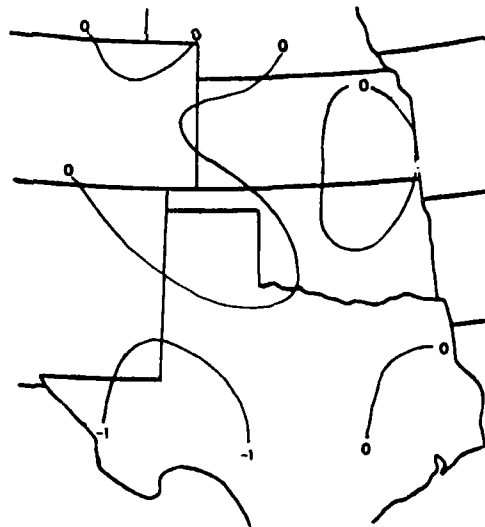


Figure 5g. 500 mb Omega ( $\mu\text{b/s}$ ) Due to Wiin-Nielsen's Deformation Function ( $F4$ ), at 1200 GMT 10 April 1979

### 3.2 Mid-morning, 10 April 1979

By 1500 GMT (Figures 6a and 6b) the cold front is slowing down in New Mexico upwind of a region of pressure falls in southeastern New Mexico. A dry line is apparent in this area and in the Pecos Valley of Texas. Visual satellite data shows Gulf Coast stratus as far northwest as Lubbock, Texas (surface dewpoint 10° C). Despite the gradual clearing of clouds in east Texas, surface winds, temperatures, and dew points indicate a strengthening warm front in the area (Figure 6a). Now three minor waves are evident in the 500 mb relative vorticity pattern (Figure 6c): No. 1 on the Kansas/Nebraska border, No. 2 in northwest Texas, and a new minor wave No. 3 in extreme west Texas. Wave No. 2 seems to be weakening.

The QG and kinematic omegas (Figures 6d and 6e) both reflect minor wave No. 3 in west Texas with a small region of ascent directly over the northern part of the surface dry line, downwind of descent near El Paso, Texas, in the area between the dry line and the cold front. Kinematic omega shows rising motion in northeast Colorado and subsidence in northwestern Oklahoma evidently associated with wave No. 1.

Kinematic omega shows ascent in south Texas near a thunderstorm area on the coast. This area moves eastward over the following six hours (Figures 6e, 7e, and 8e). Weak subsidence covers northeast Texas in Figure 6e, and skies are clearing there (Figures 5b, 6b, and 7b).

The QG omega pattern (Figure 6d) shows very little structure on the anti-cyclonic side of the 500 mb jet, which flows from southwest to northeast across west Texas and Oklahoma (Figure 6c), especially in comparison with kinematic omega (Figure 6e).

Again F3 omega (Figure 6f) approximates total QG omega (Figure 6d) closely, with some exaggeration of the values in closed centers.

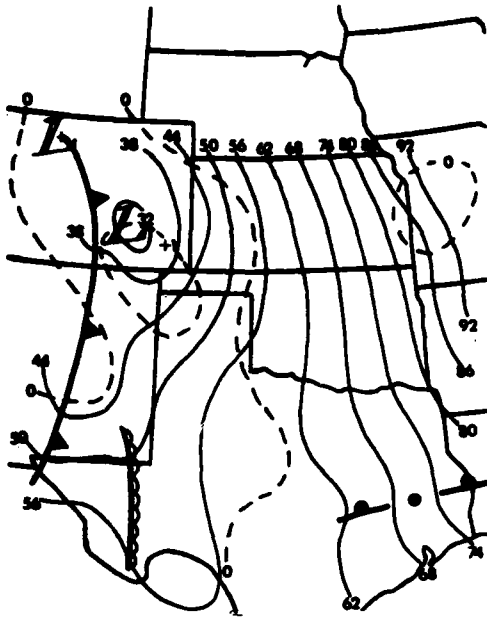


Figure 6a. Surface Fronts and Alt. Setting ( $10^2$  in Hg: solid) and Quasi-geostrophic Surface Omega ( $\mu\text{b/s}$ : dashed) at 1500 GMT 10 April 1979. Dry line (---)

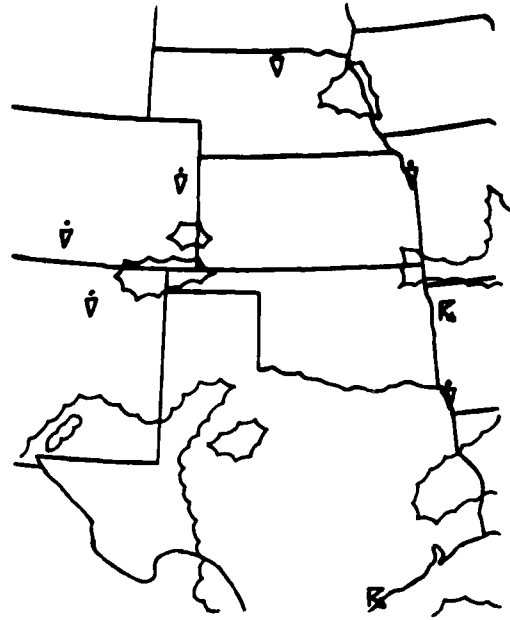


Figure 6b. Nephanalysis at 1500 GMT 10 April 1979 From GOES Video Data, With Convective and Duststorm Activity From Radar and Hourlies. Ceilings inside scallop

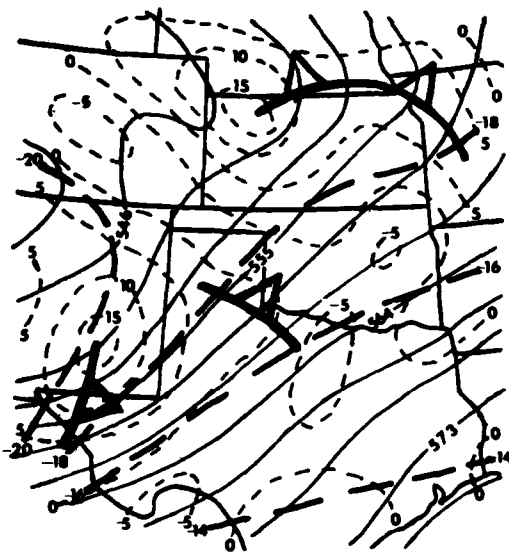


Figure 6c. 500 mb Height (m: solid lines), Temperature ( $^{\circ}\text{C}$ : heavy dashed), and Relative Vorticity ( $10^{-5} \text{ s}^{-1}$ : light dashed) at 1500 GMT. Minor wave trough (---)



Figure 6d. 500 mb Quasi-geostrophic Omega ( $\mu\text{b/s}$ ) at 1500 GMT 10 April 1979

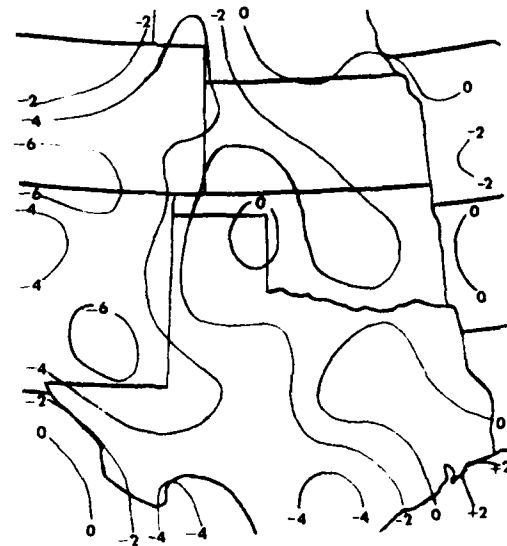


Figure 6e. 500 mb Kinematically Computed Omega ( $\mu\text{b/s}$ ) Corrected by O'Brien's Method, at 1500 GMT 10 April 1979



Figure 6f. 500 mb Omega ( $\mu\text{b/s}$ ) Due to the Advection of Vorticity ( $2\zeta + f$ ) by the Thermal Wind (F3), at 1500 GMT 10 April 1979

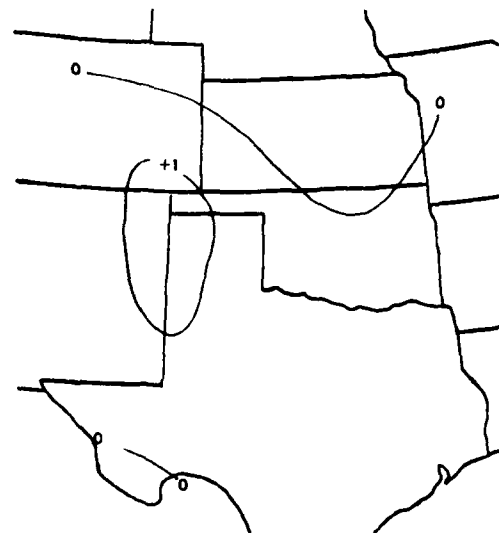


Figure 6g. 500 mb Omega ( $\mu\text{b/s}$ ) Due to Wiin-Nielsen's Deformation Function (F4), at 1500 GMT 19 April 1979

### 3.3 Noon, 10 April 1979

At 1800 GMT (Figure 7a and 7b) severe thunderstorms break out from the bulge on the dry line northward toward Amarillo, Texas. Severe storms break out also in north central Texas between the warm front and the Red River. Wink, Texas, and Carlsbad, New Mexico, first report blowing dust at 1800 GMT. Minor wave No. 2 is barely evident in the 500 mb relative vorticity pattern (Figure 7c) in northwest Oklahoma. Minor wave No. 3 is in southeastern New Mexico just upstream from the first (weak) tornado of the day (near the thunderstorm symbol in west Texas on Figure 7b). Low clouds are dissipating in southeast Colorado after at least six hours of downslope flow.

QG omega (Figure 7d) shows moderate uplift at the dry line bulge. The ascent region of kinematic omega in eastern New Mexico failed to move from 1500 to 1800 GMT (Figures 6e and 7e), but remained along the cold front, where a few thunderstorms are already occurring (Figure 7b). This is a good example of the ability of the kinematic method to pick out small regions of active convection. The kinematic omega ascent region over the Red River is remarkably timely—after many hours of rain and drizzle, this small area breaks out in hailstorms just before the time of this omega analysis (see Alberty et al),<sup>28</sup> QG omega does not show moderate ascent over this thunderstorm area until 2100 GMT (Figure 5d), three hours after kinematic omega does. Although the lower tropospheric convergence resulted in a strong upward flux of mass, moisture, and sensible heat, the transport probably was confined to a few violent thunderstorm updrafts. As a result, the 600 to 400 mb height patterns and, hence, the 500 mb QG omega pattern remained unchanged on the scale of this analysis for the first few hours of this convection.

In east Texas, QG omega subsidence disagrees with kinematic omega rising motion (Figures 7d and 7e). Kinematic omega compares better with cloudiness; after several hours of clearing in east Texas, clouds begin to thicken again after 1800 GMT and thunderstorms break out over the Texas/Louisiana border (Figures 6b, 7b, and 8b).

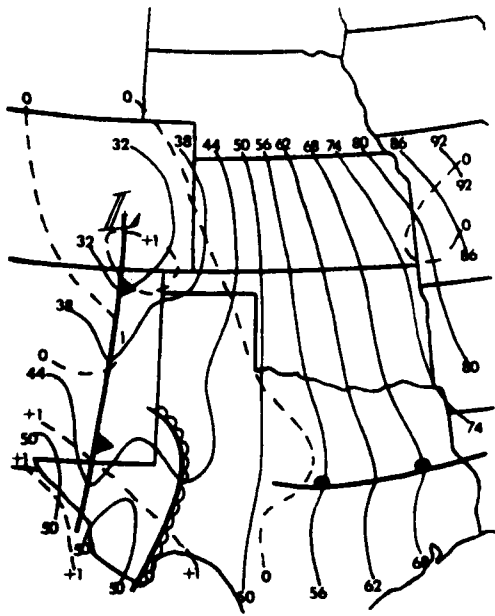


Figure 7a. Surface Fronts and Alt. Setting ( $10^2$  in Hg: solid) and Quasi-geostrophic Surface Omega ( $\mu\text{b/s}$ : dashed) at 1800 GMT 10 April 1979. Dry line ( )



Figure 7b. Nephanalysis at 1800 GMT 10 April 1979 From GOES Video Data, With Convective and Duststorm Activity From Radar and Hourlies. Ceilings inside scallop

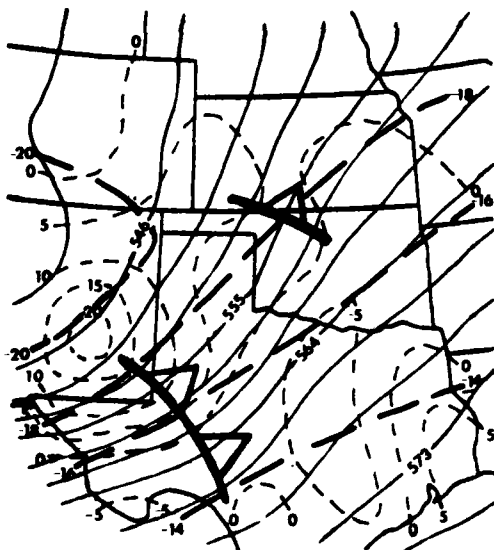


Figure 7c. 500 mb Height (m: solid lines), Temperature ( $^{\circ}\text{C}$ : heavy dashed), and Relative Vorticity ( $10^{-5} \text{ s}^{-1}$ : light dashed) at 1800 GMT. Minor wave trough ( )



Figure 7d. 500 mb Quasi-geostrophic Omega ( $\mu\text{b/s}$ ) at 1800 GMT 10 April 1979

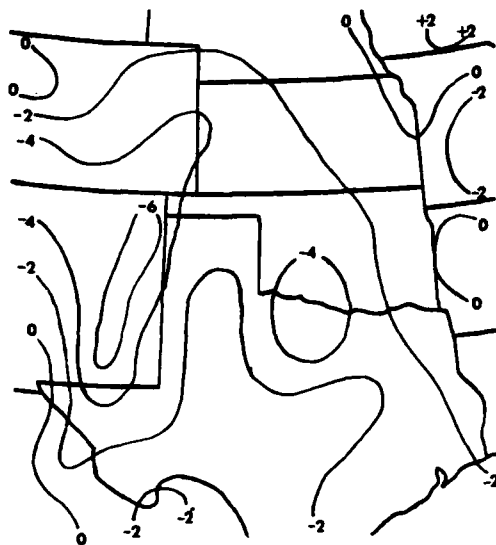


Figure 7e. 500 mb Kinematically Computed Omega ( $\mu\text{b/s}$ ) Corrected by O'Brien's Method, at 1800 GMT 10 April 1979



Figure 7f. 500 mb Omega ( $\mu\text{b/s}$ ) Due to the Advection of Vorticity ( $2\zeta + f$ ) by the Thermal Wind (F3), at 1800 GMT 10 April 1979



Figure 7g. 500 mb Omega ( $\mu\text{b/s}$ ) Due to Wiin-Nielsen's Deformation Function (F4), at 1800 GMT 10 April 1979

### 3.4 Early Afternoon, 10 April 1979

A subsynoptic surface low (SSL) develops around 2100 GMT (Figure 8a) and moves rapidly across the Texas panhandle. The clouds and weather (Figure 8b) change dramatically: a streak of wind-borne dust afflicts west Texas, a thunderstorm system which spawned tornadoes around Lubbock now spreads over the northern panhandle region, tornadic thunderstorms break out west of Wichita Falls, and a comma cloud appears over Oklahoma. A region of thunderstorms in what has become the "dry slot" of the comma cloud,<sup>9</sup> began earlier southwest of Clovis, New Mexico, and now showers are clearly visible in satellite data above the duststorm. If one extrapolates the past position of minor wave No. 2 to 2100 GMT, it should be in central Kansas in Figure 8c. It is very weak, and is not designated in that figure. Minor wave No. 3 is located in north Texas above the SSL and just north of the tornado area southwest of Wichita Falls, Texas (Figures 8a and 8b). Minor wave No. 3 is moving north-northeastward at about 30 m/sec over the SSL which is moving east-northeastward at 9 m/sec. Although positive vorticity advection would indicate pressure falls ahead of minor wave No. 3, the quasi-geostrophic pressure tendency equation allows counteracting pressure rises there if warm advection is stronger close to the ground than aloft. The rapid development of the SSL as minor wave No. 3 passed overhead and the outbreak of violent tornadoes just in the wake of the minor wave suggest that dynamical forcing associated with the mid-level disturbance influenced the low level circulation very strongly for a few hours. It will be interesting to see what happens later as minor wave No. 3 gets farther away from the SSL and warm front, and also what happens when minor waves No. 4 and No. 5 approach the front.

QG and kinematic omega (Figures 8d and 8e) appear similar. However, QG omega shows near zero vertical motion on the entire right side of the 500 mb jet running across western and northern Texas and Oklahoma (Figures 8c and 8d). This compares poorly with the comma cloud and thunderstorms in Oklahoma (Figure 8b) where kinematic omega shows ascent (Figure 8e). The reason for this major failure of the method is that the QG approximation using only F1 and F2 terms eliminates forcing due to latent heat release, which is becoming important around the convection on the right side of the jet, and also ageostrophic forcing near jet streaks.<sup>29</sup> An analysis of jet streaks and ageostrophic accelerations is beyond

29. Uccellini, L. W., and Johnson, D. R. (1979) The coupling of upper and lower troposphere jet streaks and implications for the development of severe convective storms, Mon. Wea. Res. 107:682-703.

the scope of this study; but the reader is referred to partial analyses of the same case by other authors.<sup>14, 30, 31</sup>

Kinematic omega (Figure 8e) indicates subsidence in south Texas. Skies do not clear in this region (Figure 8b); in fact, one would expect continued cloudiness under a strengthening mid-level inversion. However, a surface ridge is observed in southeast Texas beginning around 2100 GMT (Figure 8a) which is associated with two phenomena. First, the flow of moist air is shunted northwestward between Austin and San Antonio, Texas, so that a tiny area northwest of Mineral Wells, Texas, becomes extremely unstable after 2100 GMT. Second, no severe weather occurred along or south of this sharp surface ridge, probably because of the strong mid-level capping inversion.

QG omega (Figure 8d) shows subsidence just upwind of the duststorm in west Texas/New Mexico and rising motion with that portion of the comma cloud on the cyclonic side of the 500 mb jet (Figure 8c). Kinematic omega (Figure 8e) indicates a long area of moderate ascent over the entire comma cloud, centered just east of the most severe thunderstorms, and extending over the "dry slot," including the SSL. In summary, the pattern of QG omega is poorly related to the comma cloud and kinematic omega is well related during the first few hours of the comma cloud's existence.

F3 omega (Figure 8f) exaggerates QG omega (Figure 8d), but also shows a tiny subsidence region in north Texas just west of the tornadic cells (Figure 8b).

30. Benjamin, S. G., and Carlson, T. N. (1981) Numerical simulations of the severe storm environment for the 10-11 April 1979 (SESAME-I) case, in Preprints of the 12th Conference on Severe Local Storms (San Antonio), American Meteorological Society, Boston, pp 201-204.
31. Kocin, P. J., Uccellini, L. W., and Petersen, R. A. (1981) The role of jet streak "coupling" in the development of the 10-11 April 1979 Wichita Falls tornado outbreak, in Preprints of the 12th Conference on Severe Local Storms (San Antonio, American Meteorological Society, Boston, pp 560-563.

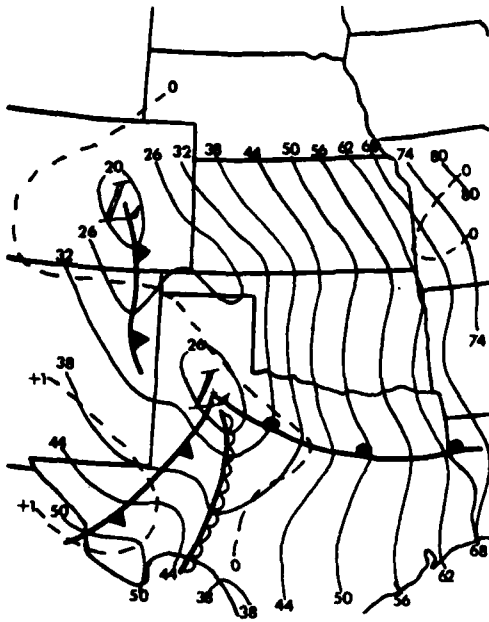


Figure 8a. Surface Fronts and Alt. Setting ( $10^2$  in Hg: solid) and Quasi-geostrophic Surface Omega ( $\mu\text{b/s}$ : dashed) at 2100 GMT 10 April 1979. Dry line (wavy line)

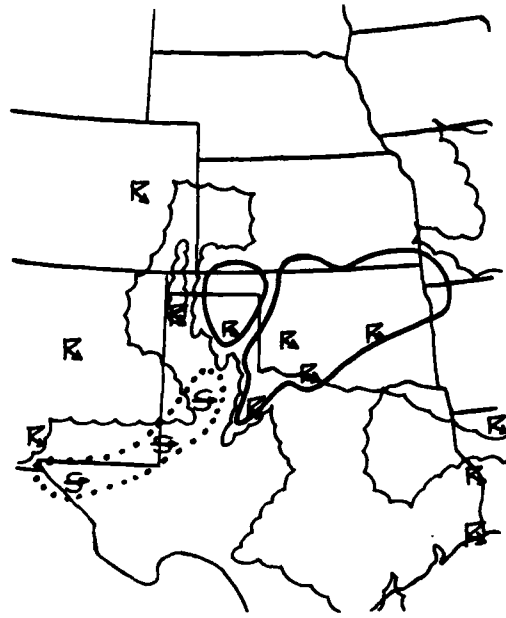


Figure 8b. Nephanalysis at 2100 GMT 10 April 1979 From GOES Video Data, With Convective and Duststorm Activity From Radar and Hourlies. Ceilings inside scallop

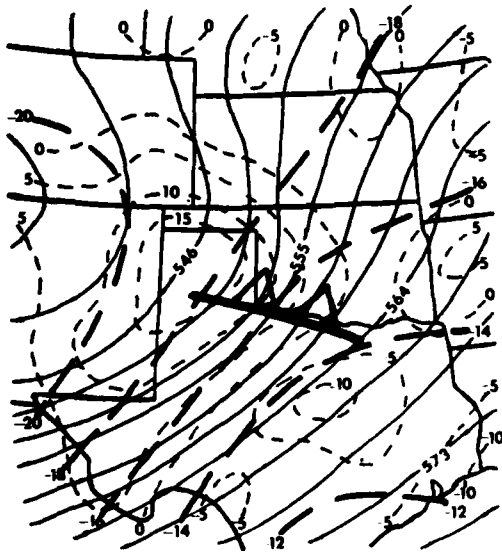


Figure 8c. 500 mb Height (m: solid lines), Temperature ( $^{\circ}\text{C}$ : heavy dashed), and Relative Vorticity ( $10^{-5} \text{ s}^{-1}$ : light dashed) at 2100 GMT. Minor wave trough (wavy line)

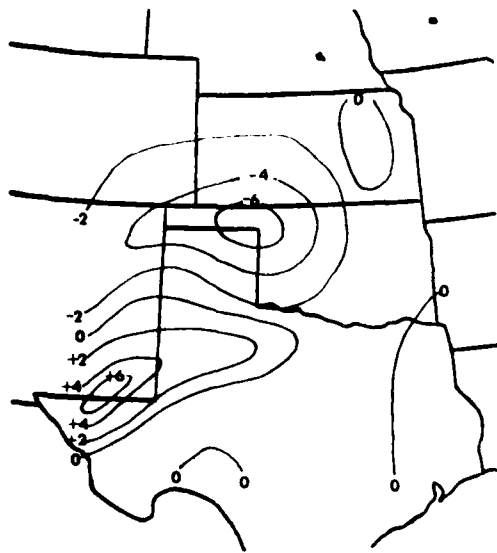


Figure 8d. 500 mb Quasi-geostrophic Omega ( $\mu\text{b/s}$ ) at 2100 GMT 10 April 1979

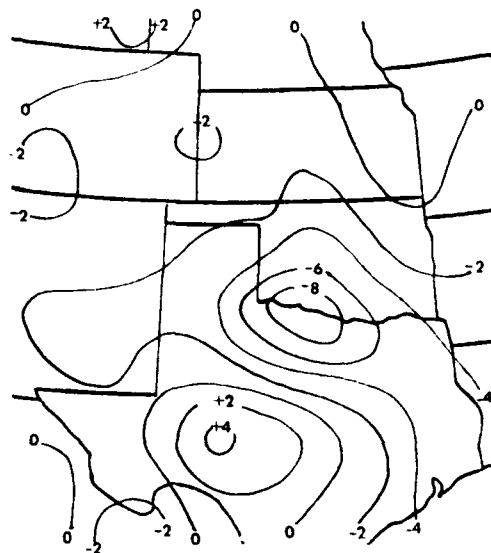


Figure 8e. 500 mb Kinetically Computed Omega ( $\mu\text{b/s}$ ) Corrected by O'Brien's Method, at 2100 GMT 10 April 1979



Figure 8f. 500 mb Omega ( $\mu\text{b/s}$ ) Due to the Advection of Vorticity ( $2\zeta + f$ ) by the Thermal Wind (F3), at 2100 GMT 10 April 1979

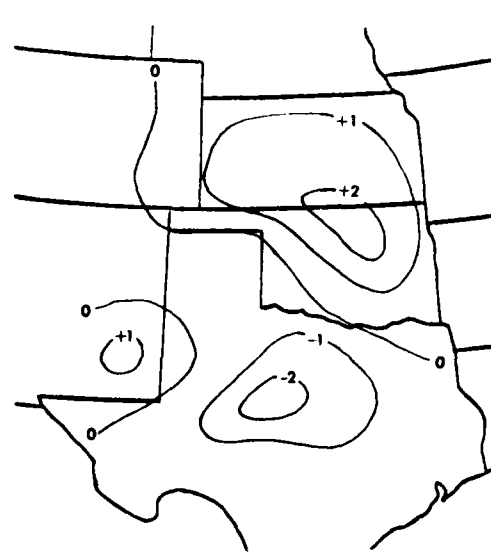


Figure 8g. 500 mb Omega ( $\mu\text{b/s}$ ) Due to Wiin-Nielsen's Deformation Function (F4), at 2100 GMT 10 April 1979

### 3.5 Late Afternoon, 10 April 1979

By 0000 GMT (Figures 9a and 9b) savage tornadoes have struck at Wichita Falls, Texas, at Lawton, Oklahoma, and at several towns in central Oklahoma. The comma cloud has tripled in area. The SSL is moving slowly and filling; the cold front and dry line move very little. A line of towering cumuli develops suddenly east of Midland, Texas, about 2300 GMT. Minor wave No. 3 is in northern Oklahoma (Figure 9c) and minor wave No. 4 appears in extreme west Texas. The most severe thunderstorms are occurring behind minor wave No. 3 in central Oklahoma and just northeast of the SSL in Texas.

QG omega (Figure 9d) shows descent over the filling SSL behind wave No. 3. The region of kinematically computed ascent in Oklahoma (Figure 9e) is much stronger and broader than the QG omega ascent area. The most significant difference in the two omega solutions is that the center of kinematic ascent lies on the 500 mb vorticity ridge of minor wave No. 3 (Figure 9c), and extends south of the wave slightly beyond the SSL and warm front in Texas. Figures 7e, 8e, 9e, and 10e indicate excellent consistency in the kinematic omega pattern, and the clouds and weather at 0000 GMT (Figure 9b) supports the kinematic analysis. Intense condensation heating in the northwestern half of Oklahoma and convergence ahead of a low-level jet<sup>14</sup> in southeast Oklahoma/northeast Texas are forcing vertical motion which QG omega cannot discern. In Figures 9b and 9e, kinematic omega shows rising motion near all active thunderstorms, including the consistent "dry slot" storms (northwest of Amarillo, Texas). One exception is the upslope area around Colorado Springs. The kinematic analysis shows ascent under the comma cloud, however it shows moderate ascent in other regions also. QG omega (Figure 9d) indicates ascent only under that part of the comma head over and west of the 500 mb jet (Figures 9b and 9c). The kinematic method gives sharp definition to the subsidence pattern just west of the developing squall line near Midland, Texas (Figures 9a and 9e).

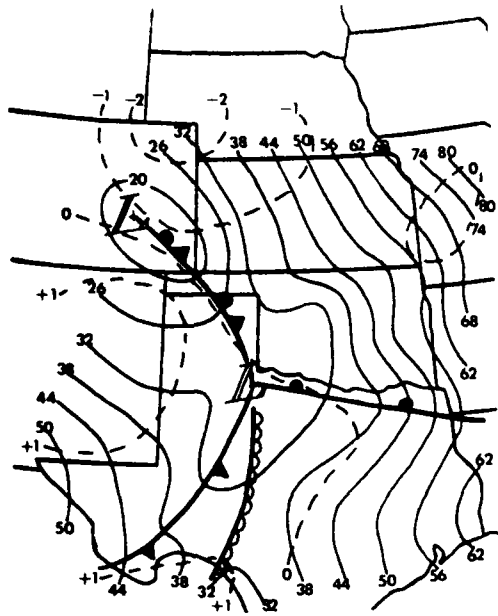


Figure 9a. Surface Fronts and Alt. Setting ( $10^2$  in Hg: solid) and Quasi-geostrophic Surface Omega ( $\mu\text{b/s}$ : dashed) at 0000 GMT 11 April 1979. Dry Line ( )

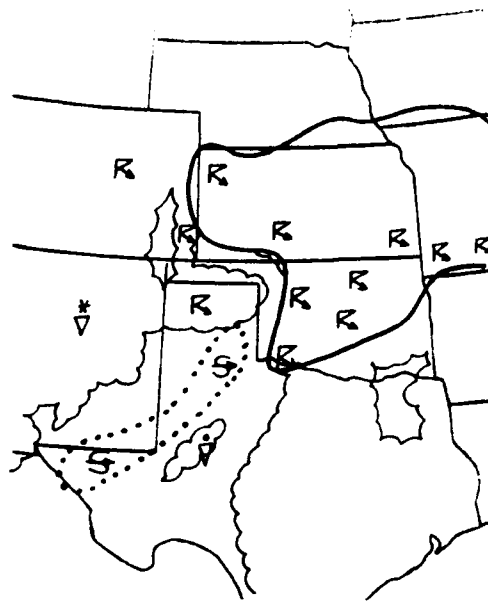


Figure 9b. Nephanalysis at 0000 GMT 11 April 1979 From GOES Video Data, With Convective and Duststorm Activity From Radar and Hourlies. Ceilings inside scallop

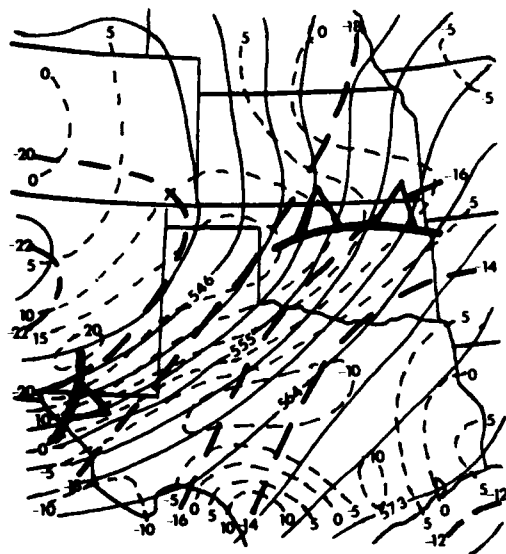


Figure 9c. 500 mb Height (m: solid lines), Temperature ( $^{\circ}\text{C}$ : heavy dashed), and Relative Vorticity ( $10^{-5} \text{ s}^{-1}$ : light dashed) at 0000 GMT. Minor wave trough ( )

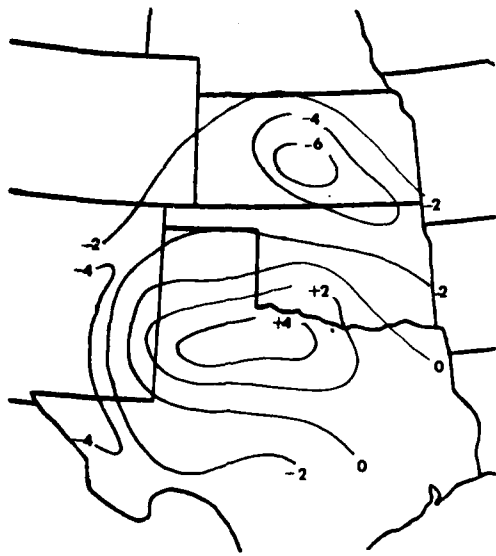


Figure 9d. 500 mb Quasi-geostrophic Omega ( $\mu\text{b/s}$ ) at 0000 GMT 11 April 1979

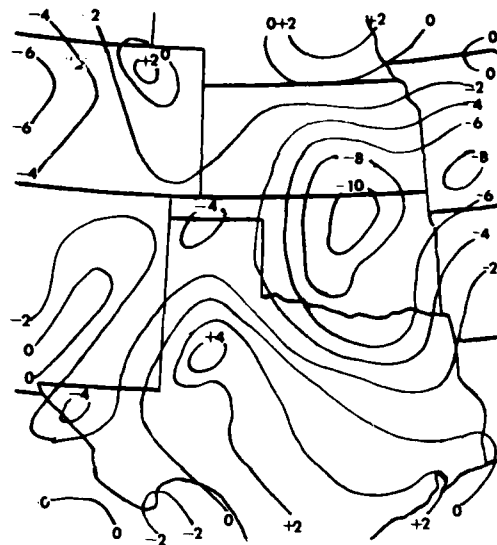


Figure 9e. 500 mb Kinematically Computed Omega ( $\mu\text{b/s}$ ) Corrected by O'Brien's Method, at 0000 GMT 11 April 1979

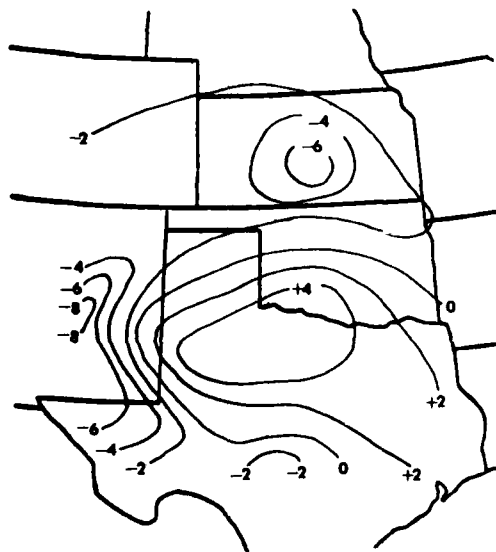


Figure 9f. 500 mb Omega ( $\mu\text{b/s}$ ) Due to the Advection of Vorticity ( $2\zeta + f$ ) by the Thermal Wind (F3), at 0000 GMT 11 April 1979

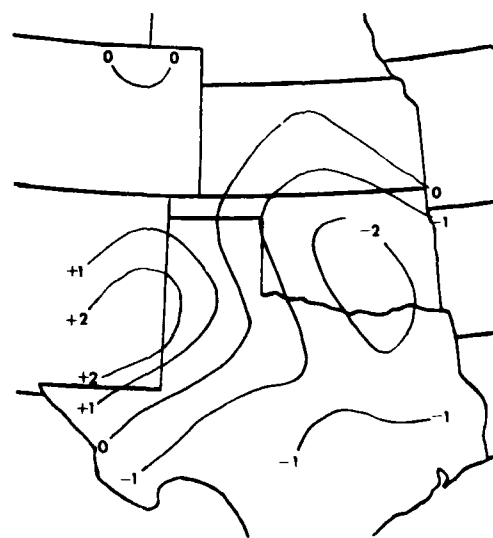


Figure 9g. 500 mb Omega ( $\mu\text{b/s}$ ) Due to Wiin-Nielsen's Deformation Function (F4), at 0000 GMT 11 April 1979

### 3.6 Evening, 10 April 1979

At 0300 GMT (Figures 10a and 10b) the SSL is nearly gone. The comma cloud doubled in size in three hours, extending westward as far as Indiana. Strong surface ridging in west Texas (Figure 10a) is associated with development of a squall line to the east (Figure 10b) which is producing large hail and some tornadoes. Severe storms continue in central Oklahoma east of the SSL along the warm front, but no damaging tornadoes are reported for a few hours. Minor wave No. 3 in southern Kansas (Figure 10c) is about 300 km past that area of weakening severe weather. Minor wave No. 4, the cold front, and the dry line all intersect at the now tornadic squall line east of Midland, Texas.

The strongest QG omega ascent analyzed in this data set ( $9 \mu\text{b/s}$ ) is in Kansas in a region of little or no convective activity (Figures 10b and 10d). It encompasses the part of the comma head west of the 500 mb jet (Figure 10c), but it also invades the dry slot where one might expect subsidence. Kinematic omega (Figure 10e) shows most of the comma in a region of 500 mb ascent; however, it shows moderate dry slot ascent, similar to the QG solution. The comma extends northeastward over a region of subsidence in Iowa. QG omega does not show much ascent over the strong convection in southwest Missouri, although kinematic omega does. Both solutions show moderate or better ascent associated with the minor wave in southern Kansas with an important difference: QG omega shows ascent changing to descent as the upper wave passes, while kinematic omega shows strong ascent centered on the troughline of the minor wave, extending several hundred kilometers upstream of the trough. QG omega shows subsidence behind wave No. 4 in west Texas, but kinematic omega shows rising motion there (Figures 10c, 10d, and 10e). The surface ridge in south Texas (Figure 10a) shifts southward under continued (kinematically computed) subsidence.

Beginning at this time, QG omega (Figure 10d) shows intense subsidence over west Texas and southern New Mexico in contradiction to kinematic omega (Figure 10e). Diabatic cooling of the surface in the evening would intensify subsidence, so some other ageostrophic forcing must account for this unreasonable QG result. The area is also the scene of moderate F4 (deformation-induced) forcing (Figure 10g). It is interesting to note the similarity between this case and another case which Krishnamurti<sup>21</sup> analyzed with QG and balance omega equations. In both cases, as an open, developing wave began occluding, cold advection in the base of the 500 mb trough forced strong QG subsidence (see Figures 14l, 14n, and so on). Krishnamurti showed that the contribution by the laplacian of thermal advection in the balance omega equation showed strong subsidence there, but that two ageostrophic forcing

terms together compensated for approximately half of this thermally-induced subsidence. These terms were the "differential deformation" and "differential divergence" effects. Either or both of these effects may have compensated for strong cold-advection subsidence on 11 April 1979 as well.

F3 omega (Figure 10f) begins to have significant deviations from QG omega (Figure 10g) at this time. In its analysis in west Texas, Kansas, and Oklahoma, QG omega complements the cloud and weather patterns (Figures 10b and 10d) less and less. So this failure of Wiin-Nielsen's method to approximate QG omega comes at a time in the storm's evolution when QG omega itself is not well related to the observed clouds and weather.

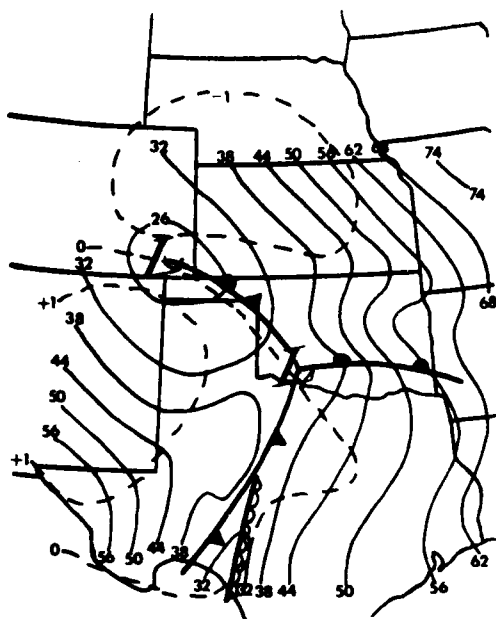


Figure 10a. Surface Fronts and Alt. Setting ( $10^2$  in Hg: solid) and Quasi-geostrophic Surface Omega ( $\mu\text{b/s}$ : dashed) at 0300 GMT 11 April 1979. Dry line (wavy line)

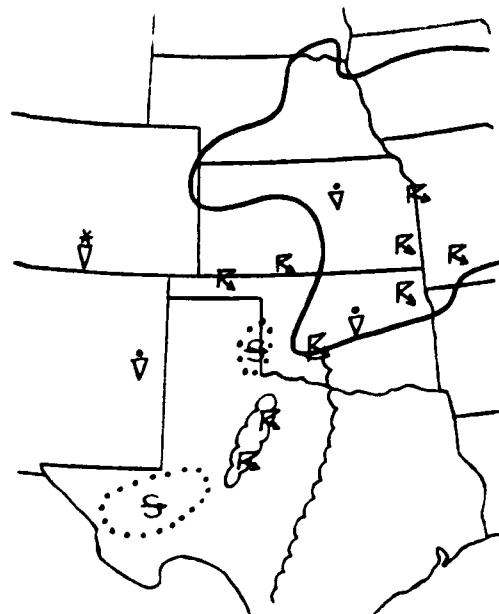


Figure 10b. Nephanalysis at 0300 GMT, 11 April 1979 From GOES IR Data, With Convective and Duststorm Activity From Radar and Hourlies. Ceilings inside scallop

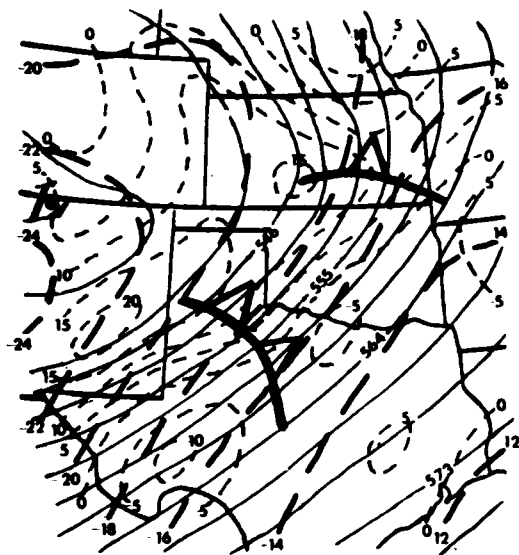


Figure 10c. 500 mb Height (m: solid lines), Temperature ( $^{\circ}\text{C}$ : heavy dashed), and Relative Vorticity ( $10^{-5} \text{ s}^{-1}$ : light dashed) at 0300 GMT. Minor wave trough (wavy line)

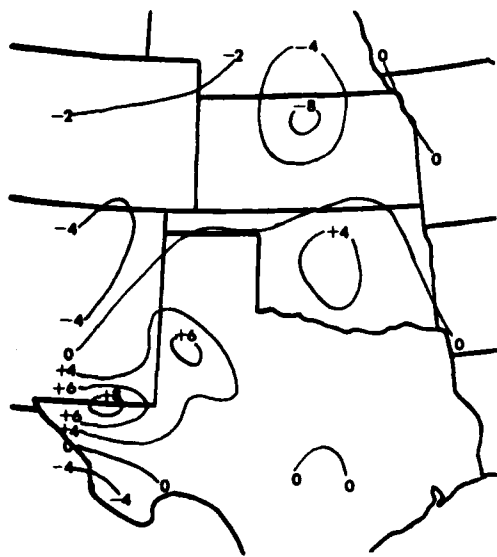


Figure 10d. 500 mb Quasi-geostrophic Omega ( $\mu\text{b/s}$ ) at 0300 GMT 11 April 1979

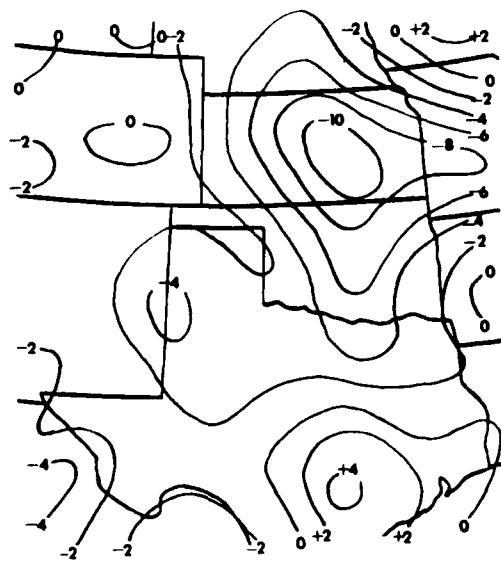


Figure 10e. 500 mb Kinematically Computed Omega ( $\mu\text{b/s}$ ) Corrected by O'Brien's Method, at 0300 GMT 11 April 1979

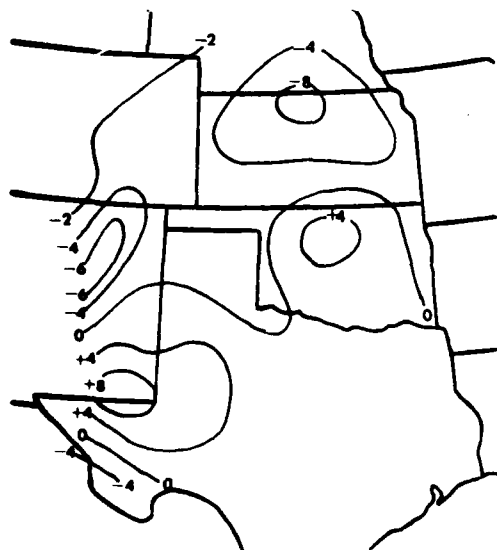


Figure 10f. 500 mb Omega ( $\mu\text{b/s}$ ) Due to the Advection of Vorticity ( $2\xi + f$ ) by the Thermal Wind (F3), at 0300 GMT 11 April 1979

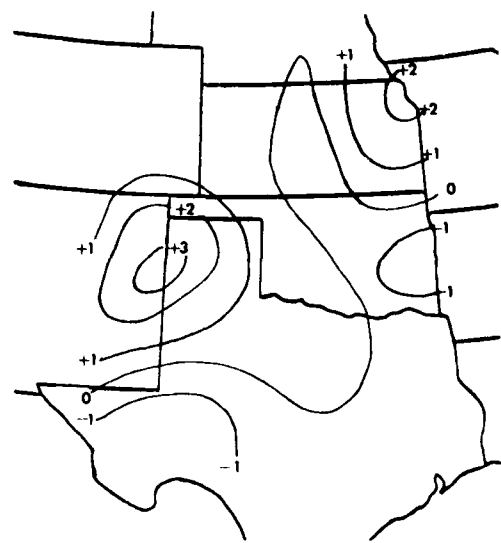


Figure 10g. 500 mb Omega ( $\mu\text{b/s}$ ) Due to Wiin-Nielsen's Deformation Function (F4), at 0300 GMT 11 April 1979

### 3.7 Midnight, 10-11 April 1979

The SSL is gone by 0600 GMT (Figures 11a and 11b), and the cold front slows down in central Texas. The squall line in north Texas becomes coincident with the tail of the comma cloud. Thunderstorms persist in the dry slot of the comma cloud. Three minor waves are evident in the 500 mb relative vorticity pattern (Figure 11c). Wave No. 3 is on the Kansas/Nebraska border, wave No. 4 is in western Oklahoma, and wave No. 5 is in southeastern New Mexico. Although some severe weather continues in northeastern Oklahoma, the most severe thunderstorms are occurring at the intersection of minor wave No. 4 with the warm front, and behind wave No. 4 along the cold front in central Texas.

The QG and kinematic omega fields are not even remotely similar at this time (Figures 11d and 11e). The QG pattern is generally perpendicular to the comma cloud tail, and some of the active thunderstorms are in areas of QG omega subsidence (Figure 11b). The kinematic omega pattern is very similar to the comma cloud except that (1) the strongest kinematic ascent is along the poleward side of the comma tail, and (2) the part of the comma head to the left of the 500 mb jet (Figure 11c) is indicated as subsiding. Thus, the center line of the comma tail is slightly downwind (northeast) of the axis of maximum kinematically-computed 500 mb ascent. The strongest ascent of the entire data set ( $13 \mu\text{b/s}$ ) is analyzed 200 km northwest of the nose of the dry slot.

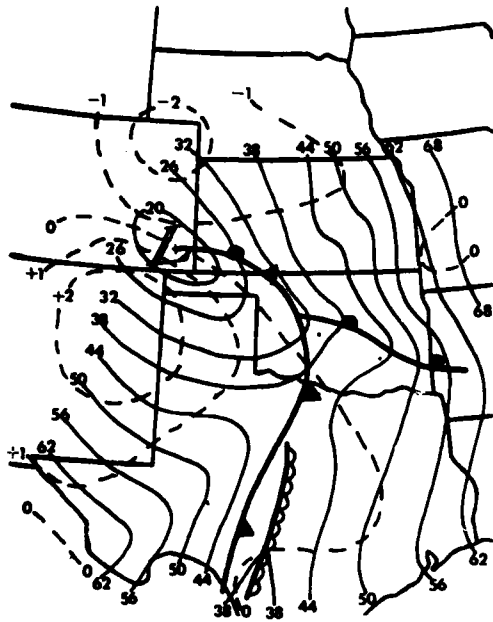


Figure 11a. Surface Fronts and Alt. Setting ( $10^2$  in Hg: solid) and Quasi-geostrophic Surface Omega ( $\mu\text{b/s}$ : dashed) at 0600 GMT 11 April 1979 Dry line (  )



Figure 11b. Nephanalysis at 0600 GMT 11 April 1979 From GOES IR Data, With Convective and Duststorm Activity From Radar and Hourlies. Ceilings inside scallop

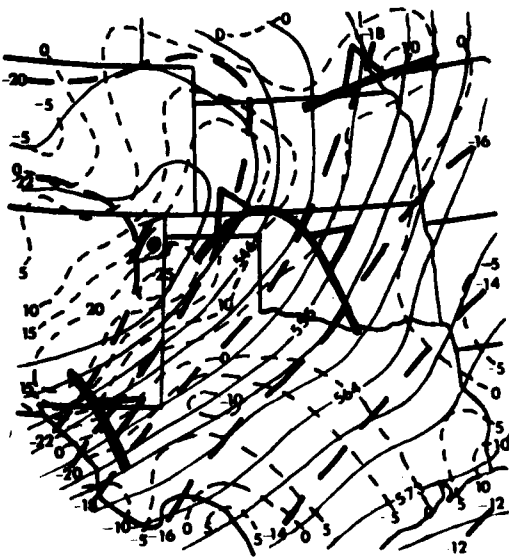


Figure 11c. 500 mb Height (m: solid lines), Temperature ( $^{\circ}\text{C}$ : heavy dashed), and Relative Vorticity ( $10^{-5} \text{ s}^{-1}$ : light dashed) at 0600 GMT. Minor wave trough (  )



Figure 11d. 500 mb Quasi-geostrophic Omega ( $\mu\text{b/s}$ ) at 0600 GMT 11 April 1979

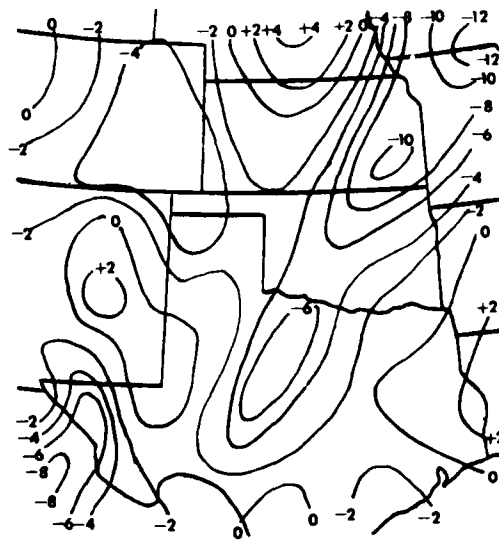


Figure 11e. 500 mb Kinematically Computed Omega ( $\mu\text{b/s}$ ) Corrected by O'Brien's Method, at 0600 GMT 11 April 1979



Figure 11f. 500 mb Omega ( $\mu\text{b/s}$ ) Due to the Advection of Vorticity ( $2\zeta + f$ ) by the Thermal Wind (F3), at 0600 GMT 11 April 1979

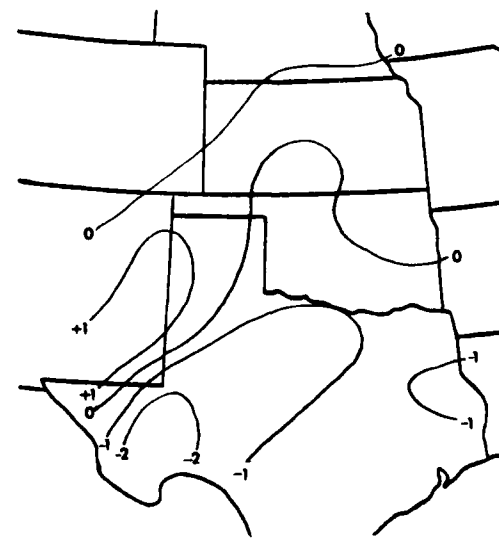


Figure 11g. 500 mb Omega ( $\mu\text{b/s}$ ) Due to Wiin-Nielsen's Deformation Function (F4) at 0600 GMT 11 April 1979

### 3.8 Early Morning, 11 April 1979

A mesolow forms where the cold front nears the Texas/Oklahoma border at 0900 GMT (Figure 12a). Both minor wave No. 4 in northern Kansas and minor wave No. 5 in west Texas are too distant from this region to account for this development (Figure 12c). The squall line in central Texas is moving northeastward, well north of the surface ridge on the Texas coastal plains (Figures 12a and 12b). Less severe weather in eastern Oklahoma and north Texas was reported at this time of the morning than in earlier hours.

Kinematic omega (Figure 12e) conforms to the comma cloud pattern very well (Figure 12b), except that the ascent in Texas is much more widespread than the clouds and thunderstorms. There has been a consistent pattern since the comma cloud first appeared around 2100 GMT (see Figures 8b/8e, 9b/9e, 10b/10e, 11b/11e, and 12b/12e) for kinematic omega to indicate ascent south and southeast of the tip of the comma cloud and for the comma cloud tail to grow toward the southwest with the repeated squall lines in north Texas. Most of the comma cloud advects downstream very rapidly, but the tip of the comma cloud tail stays in north Texas in a region of rising motion. QG omega (Figure 12d) shows descent just northeast of an active squall line in north Texas and ascent over all of the dry slot (Figure 12b). There is a single thunderstorm in the dry slot, but the kinematically computed descent (Figure 12e) over most of the dry slot looks believable. In northern New Mexico, downslope winds (see the surface omega in Figure 12a) are reflected in the kinematic omega but not in QG omega.

F3 omega (Figure 12f) seems to moderate the QG omega maximum. Recall that F3 omega normally overestimates QG maxima. F4 omega (Figure 12g) rises to  $+4 \mu\text{b/s}$  near a  $35 \times 10^{-5} \text{ s}^{-1}$  relative vorticity maximum in New Mexico.

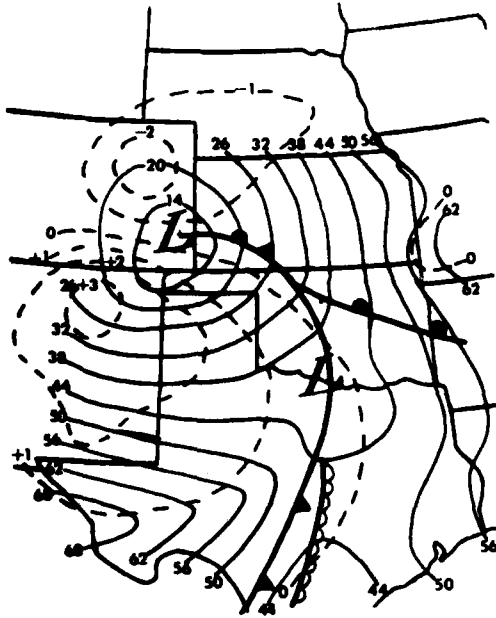


Figure 12a. Surface Fronts and Air Setting ( $10^2$  in Hg: solid) and Quasi-geostrophic Surface Omega ( $\mu\text{b/s}$ : dashed) at 0900 GMT 11 April 1979. Dry line (  )

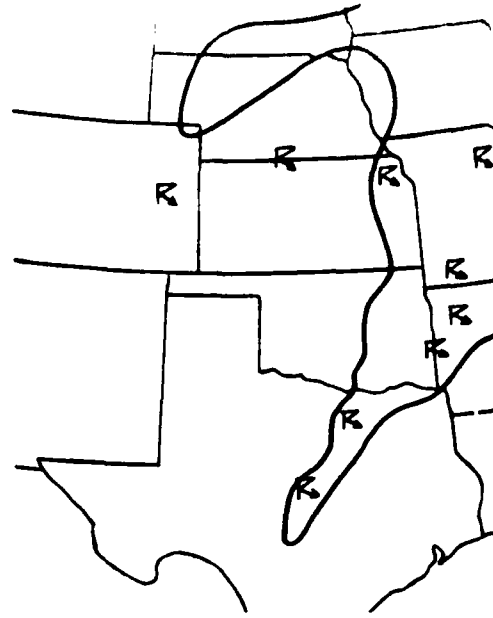


Figure 12b. Nephanalysis at 0900 GMT 11 April 1979 From GOES IR Data, With Convective and Duststorm Activity From Radar and Hourlies



Figure 12c. 500 mb Height (m: solid lines), temperature ( $^{\circ}\text{C}$ : heavy dashed), and Relative Vorticity ( $10^{-5} \text{ s}^{-1}$ : light dashed) at 0900 GMT. Minor wave trough (  )



Figure 12d. 500 mb Quasi-geostrophic Omega ( $\mu\text{b/s}$ ) at 0900 GMT 11 April 1979

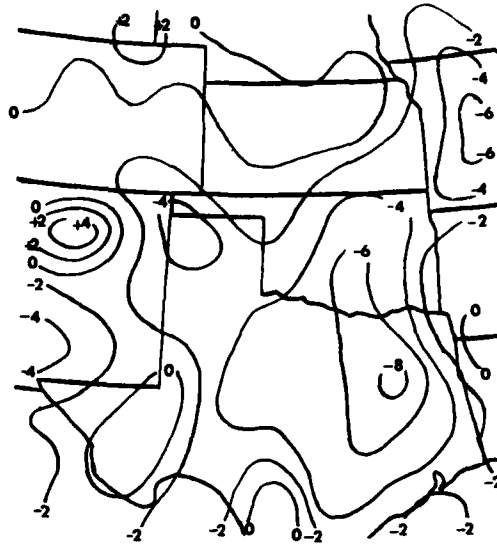


Figure 12e. 500 mb Kinematically Computed Omega ( $\mu\text{b/s}$ ) Corrected by O'Brien's Method, at 0900 GMT 11 April 1979



Figure 12f. 500 mb Omega ( $\mu\text{b/s}$ ) Due to the Advection of Vorticity ( $2\zeta+f$ ) by the Thermal Wind (F3), at 0900 GMT 11 April 1979

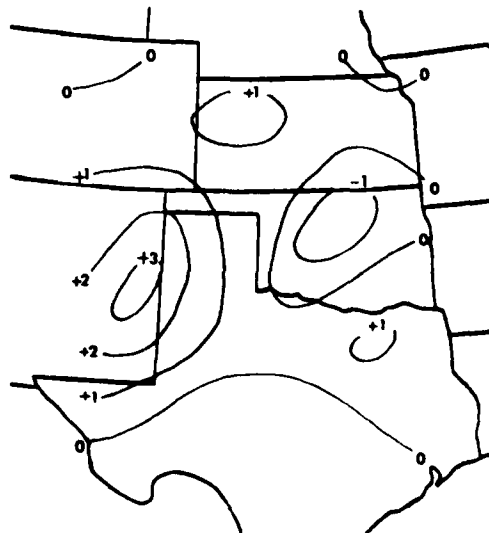


Figure 12g. 500 mb Omega ( $\mu\text{b/s}$ ) Due to Wiin-Nielsen's Deformation Function (F4), at 0900 GMT 11 April 1979

### 3.9 Dawn, 11 April 1979

By 1200 GMT (Figures 13a and 13b) most of the comma cloud has moved out of the analysis region. Very little severe convection continues. However, minor wave No. 5 (Figure 13c) is in central Texas approaching the mesolow on the cold front. At this point, one might forecast renewed severe weather activity east and northeast of this mesolow beginning about the time wave No. 5 would be above the mesolow (say, 1830 GMT). Severe weather did break out again at 1850 GMT south-southeast of the mesolow, and it spread northeastward into Oklahoma, Louisiana, and Arkansas during 11 April 1979.<sup>28</sup>

Again, QG omega (Figure 13d) seems unrelated to the comma cloud, thunderstorm, or kinematic omega patterns. Kinematic omega (Figure 13e) compares very favorably with clouds and weather (Figure 13b).

F3 omega (Figure 13f) exaggerates QG omega (Figure 13d) in an analyzed ascent area in central New Mexico. A maximum of relative vorticity (Figure 13c) dominates the F4 omega pattern (Figure 13g)

### 3.10 The Traditional Partition of Quasi-geostrophic Omega

Figure 14 contains fields of F1 and F2 omega for each of the nine data sets. Initially, F1 and F2 omega tend to cancel one another (see Trenberth)<sup>24</sup> except near strong centers where one or the other dominates. Thus QG omega is often smaller in absolute value than either F1 or F2 omega, except in rather isolated centers of activity. In Figures 5d, 6d, 7d, and so on, QG omega has large areas between +2 and -2  $\mu\text{b/s}$ , but in Figure 14 many of these same areas have more intense F1 and F2 omega.

Moreover, although F1 omega may dominate F2 omega at one time in an area where QG omega is moderate to strong, three to six hours later F2 omega may dominate F1 omega, or vice-versa. For example, a maximum of QG omega from 1200 to 1800 GMT in extreme west Texas (Figures 5d, 6d, and 7d) results at 1200 GMT from F2 omega (Figure 14b), at 1500 GMT equally from F1 and F2 omega (Figures 14c and 14d), and at 1800 GMT from F1 alone (Figure 14e). Sometimes the change is synoptically reasonable. As early as 1200 GMT, 500 mb F1 omega ascent in eastern New Mexico (Figure 14a) presages the development of an SSL in west Texas around 2100 GMT. The QG pattern in this area is dominated first by F1, then suddenly at 1800 GMT (Figures 14e and 14f) by F2 as warm advection increases across Texas.

At other times, intense and opposed centers of F1 and F2 activity (Figures 14k and 14l in Oklahoma; Figures 14m and 14n in west Texas) resolve into a single maximum of QG omega (Figures 10d and 11d). From 2100 to 0300 GMT, QG omega (Figures 8d, 9d, and 10d) exhibits a much less complicated pattern than either F1 or F2 omega (Figures 14g through 14l).

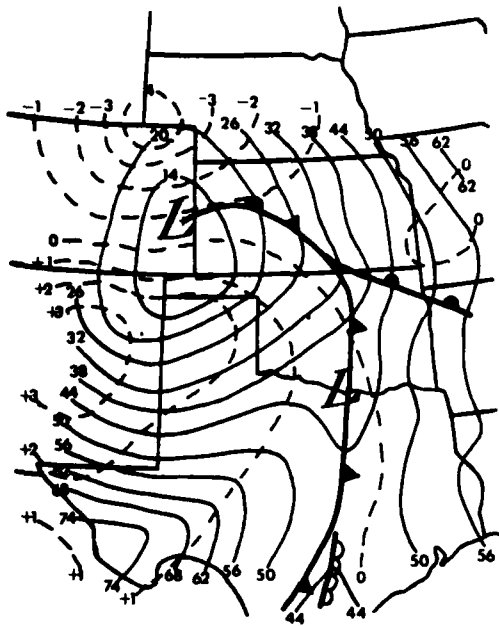


Figure 13a. Surface Fronts and Alt. Setting ( $10^2$  in Hg: solid) and Quasi-geostrophic Surface Omega ( $\mu\text{b/s}$ : dashed) at 1200 GMT 11 April 1979. Dry line (.....)



Figure 13b. Nephanalysis at 1200 GMT 11 April 1979 From GOES IR Data, With Convective and Duststorm Activity From Radar and Hourlies



Figure 13c. 500 mb Height (m: solid lines), Temperature ( $^{\circ}\text{C}$ : heavy dashed), and Relative Vorticity ( $10^{-5} \text{ s}^{-1}$ : light dashed) at 1200 GMT. Minor wave trough (~~~~)

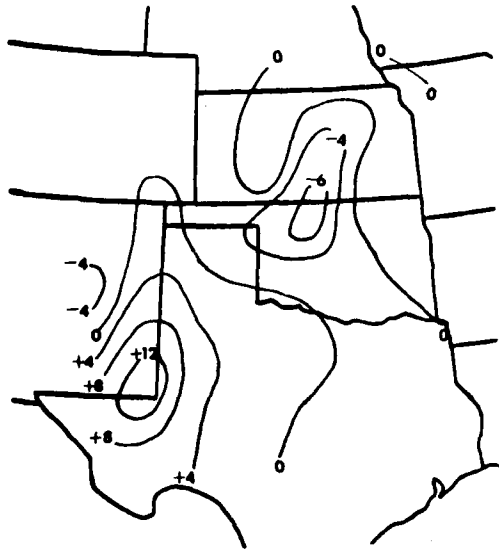


Figure 13d. 500 mb Quasi-geostrophic Omega ( $\mu\text{b/s}$ ) at 1200 GMT 11 April 1979

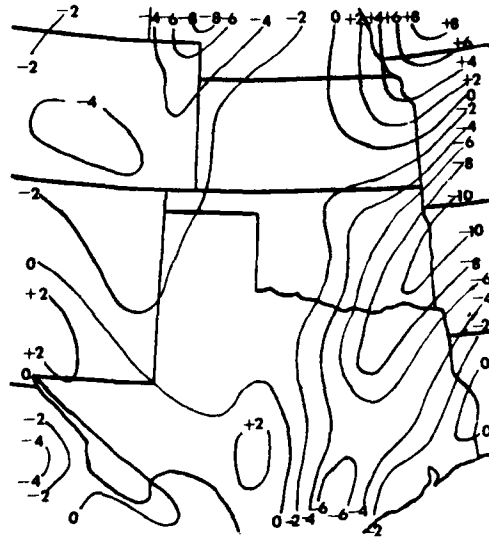


Figure 13e. 500 mb Kinematically Computed Omega ( $\mu\text{b/s}$ ) Corrected by O'Brien's Method, at 1200 GMT 11 April 1979

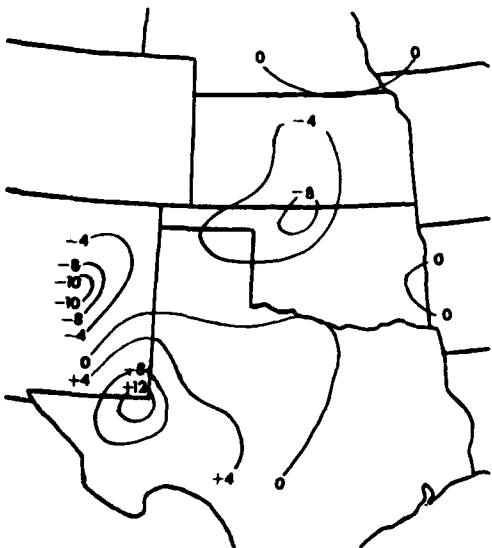


Figure 13f. 500 mb Omega ( $\mu\text{b/s}$ ) Due to the Advection of Vorticity ( $2\zeta+f$ ) by the Thermal Wind ( $F3$ ), at 1200 GMT 11 April 1979

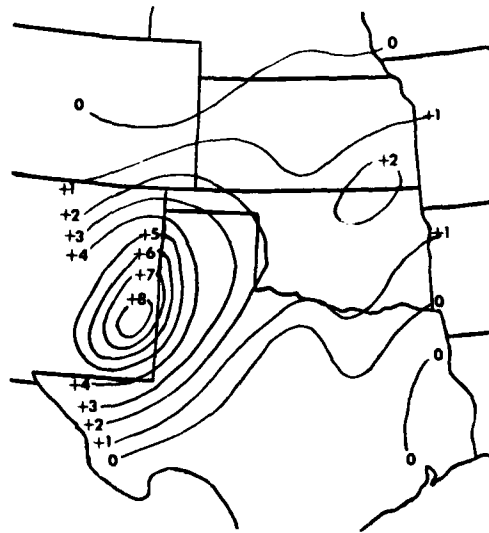


Figure 13g. 500 mb Omega ( $\mu\text{b/s}$ ) Due to Wiin-Nielsen's Deformation Function ( $F4$ ), at 1200 GMT 11 April 1979



Figure 14a. 500 mb Omega ( $\mu\text{b/s}$ ) Due to Differential Vorticity Advection (F1), at 1200 GMT 10 April 1979

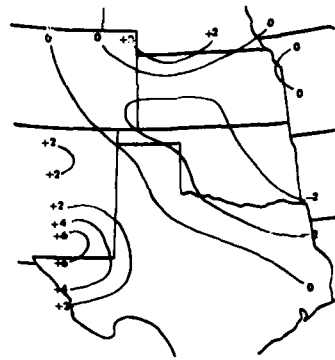


Figure 14b. 500 mb Omega ( $\mu\text{b/s}$ ) Due to the Laplacian of Temperature Advection (F2), at 1200 GMT 10 April 1979



Figure 14c. Same as Figure 14a Except 1500 GMT 10 April 1979



Figure 14d. Same as Figure 14b Except 1500 GMT 10 April 1979



Figure 14e. Same as Figure 14a Except 1800 GMT 10 April 1979



Figure 14f. Same as Figure 14b Except 1800 GMT 10 April 1979

Figure 14. Traditional Partition of Quasi-geostrophic Omega for All Nine Analyses



Figure 14g. Same as Figure 14a Except  
2100 GMT 10 April 1979



Figure 14h. Same as Figure 14b Except  
2100 GMT 10 April 1979



Figure 14i. Same as Figure 14a Except  
0000 GMT 11 April 1979

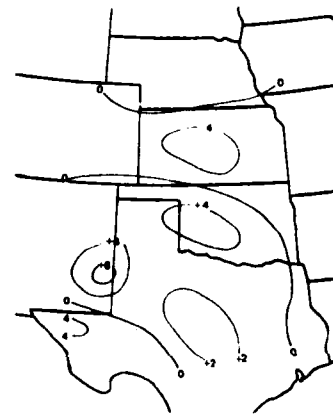


Figure 14j. Same as Figure 14b Except  
0000 GMT 11 April 1979

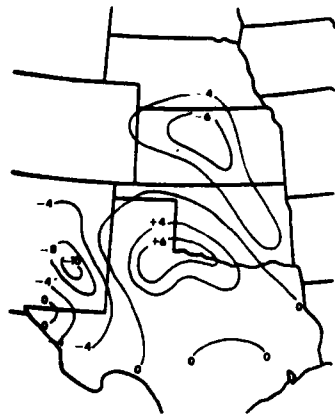


Figure 14k. Same as Figure 14a Except  
0300 GMT 11 April 1979

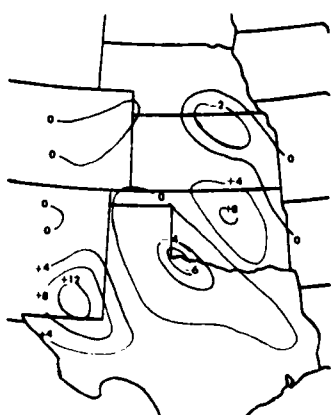


Figure 14l. Same as Figure 14b Except  
0300 GMT 11 April 1979



Figure 14m. Same as Figure 14a Except  
0600 GMT 11 April 1979

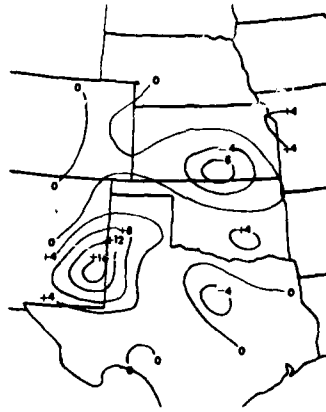


Figure 14n. Same as Figure 14b Except  
0600 GMT 11 April 1979

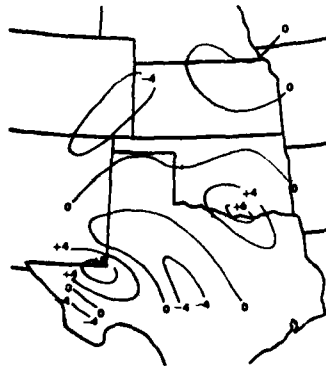


Figure 14o. Same as Figure 14a Except  
0900 GMT 11 April 1979

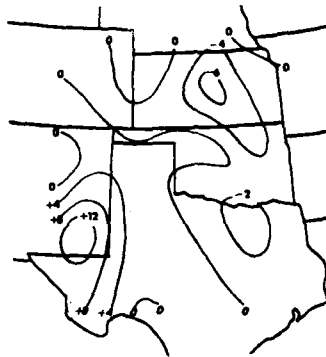


Figure 14p. Same as Figure 14b Except  
0900 GMT 11 April 1979



Figure 14q. Same as Figure 14a Except  
1200 GMT 11 April 1979

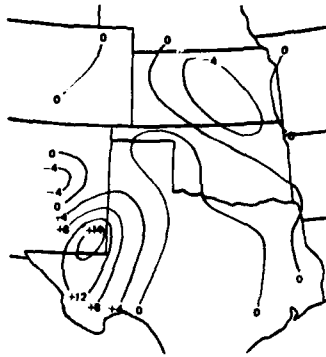


Figure 14r. Same as Figure 14b Except  
1200 GMT 11 April 1979

#### 4. CONCLUSIONS AND RECOMMENDATIONS

Five mid-level disturbances of wavelength 500 to 800 km passed through the area at speeds of 20 to 33 m/sec, evident in strong variations of mid-level height, vorticity, and vertical motion. The 500 mb quasi-geostrophic (QG) omega field often showed ascent followed by subsidence as these disturbances passed, while kinematically computed omega showed strong ascent on the trough-line of these disturbances. The "minor" short waves were associated with movement of the subsynoptic surface low (SSL) and dry line, with development and filling of the SSL, with the location and onset of severe storms, and with major features of the comma cloud. As two of these waves passed the SSL or the cold front/dry line intersection in central Texas, severe thunderstorms broke out or intensified just northeast through southeast of the surface low and remained violent until the waves were several hundred kilometers downstream.

A comparison of clouds and weather to vertical motion computed by the kinematic method (with O'Brien's correction) and the QG omega equation method, indicates that both methods are able to resolve detail in weather phenomena as small as three gridlengths (480 km). However, QG omega became very inaccurate as ageostrophic processes became stronger during the evolution of the storm system. In fact, both methods give spurious results at times. The discrepancy between the two omega solutions was probably a result of physical forcing not considered in the simplified QG omega equation, namely latent heat release and ageostrophic response in general, as well as to errors in the observed wind fields. One can draw the following conclusions: for research purposes these methods make an independent and complementary pair, while for operational purposes the computational ease and ageostrophic sensitivity of the kinematic method make it preferable to the QG method.

The QG method appeared to fail in many situations. It grossly overestimated the subsidence region in southern New Mexico southwest of the closing upper low. Krishnamurti's<sup>21</sup> solution of the balance wind omega equation for a very similar synoptic situation showed an almost identical subsidence region forced by cold advection, which was counterbalanced by two ageostrophic forcing functions: differential deformation and differential divergence. The QG method consistently analyzed 500 mb ascent under that portion of the comma "head" to the left of the jet, but elsewhere failed. In general, the QG analysis did not recognize significant vertical motion on the anticyclonic side of the 500 mb jet. One may infer, tentatively, that vertical motion due to latent heat release and to ageostrophic forcing on the right of the mid-tropospheric jet became as significant as the QG forces. In particular, other researchers<sup>14, 31</sup> have found evidence that the accelerations in the region of a jet streak became important on 10-11 April 1979. As shown in

Uccellini and Johnson,<sup>29</sup> strong upward motion occurs in the low levels of jet streak exit regions, induced by ageostrophic forces.

Kinematic omega consistently analyzed rising motion in active thunderstorm areas. Its ability to locate ascent forced by physical factors neglected in the QG omega equation which was solved, especially latent heat release and ageostrophic accelerations under the exit region of a jet streak, establish the kinematic method as definitely superior to the QG method for forecasting purposes. Sometimes, kinematic omega indicated ascent in an area before thunderstorms occurred. The relationship of kinematically computed omega to the comma cloud can be summarized as follows:

(1) Kinematic omega is always centered in the active convection on the western edge of the comma's tail, so that the center line of the comma tail advected in time slightly east of the axis of maximum instantaneous rising motion.

(2) New centers of ascent formed repeatedly southeast and south of the comma tail before the tail extended over these new convection regions.

(3) Kinematic calculations indicated that omega in the "dry slot" varies considerably, but tended to be upward around the consistently observed dry slot thunderstorms.<sup>9</sup> The sharp back edge of comma cloud can not be taken as a dividing line between instantaneous descent and ascent.

(4) Kinematic omega usually indicates rising motion under that portion of the comma head to the left of the 500 mb jet; however, in one analysis (0600 GMT) the opposite was true.

A comparison of QG omega with F3 omega, the part due to the advection of vorticity by the thermal wind, shows very strong qualitative agreement. However, F3 omega tends to exaggerate QG omega up to 25 percent in closed maxima or minima. The difference between the two, which is motion forced by F4 omega or Wiin-Nielsen's deformation function, became significant in certain areas after the storm began occluding around 0300 GMT. At about the same time, QG omega began to show gross errors in comparison to kinematic omega and to clouds and weather. The very largest values of F4 omega were associated with intense relative vorticity maxima in the cold core of the 500 mb low.

Two details of this analysis apply specifically to forecasting severe thunderstorms in the southern plains in springtime. First, both the kinematic and the QG analyses showed an area of 500 mb rising motion in eastern New Mexico at least six hours before an SSL and tornadoes formed just to the east in Texas. Second, prolonged subsidence over the Texas coastal plain caused surface pressure ridging and the maintenance of an intense mid-level inversion. These features simultaneously suppressed convection in southeast Texas and diverted moisture northwest of the region.

There are several areas for further study that are recommended. Many subtle mechanisms in this storm are contained in its three-dimensional structures of horizontal wind, vertical motion, and other parameters. A complete analysis, particularly a three-dimensional analysis of moisture, clouds, and weather, could provide a definitive portrait of the evolution of the system. This study highlights three points of departure. First, more information about the structure of mesa- $\alpha$  scale upper disturbances which are termed "minor waves" in this study and their relationship to the low level circulation and weather is necessary to the understanding of the organization of severe weather patterns. The problem of detecting and forecasting these waves is important. Operational forecasters have had some success at the analysis task by subjectively combining conventional rawinsonde data with surface and radar reports (see Miller)<sup>32</sup> and with satellite data (see Miller and McGinley).<sup>1</sup> Second, the implications of ageostrophic accelerations in the exit region of jet streaks need to be explored and modeled on smaller scales (meso- $\alpha$  or meso- $\beta$ ) than heretofore.<sup>29</sup> Third, a fully integrated moisture and cloud analysis every three hours would be an ideal verification tool for all types of cloud forecasting techniques.

---

32. Miller, R. C. (1975) Notes on Analysis and Severe-Storm Forecasting Procedures of the Air Force Global Weather Central, AWS TR 200 (Revised), Chapters 1, 4, and 11.

## References

1. Miller, R. C., and McGinley, J. A. (1977) Using Satellite Imagery to Detect and Track Comma Clouds and the Application of the Zone Technique in Forecasting Severe Storms, GE/MATSCO, Beltsville, MD, 96 pp.
2. Boucher, R. J., and Newcomb, R. J. (1962) Synoptic interpretation of some TIROS vortex patterns: a preliminary cyclone model, J. Appl. Meteor. 1:127-136.
3. Timchalk, A., and Hubert, L. F. (1961) Satellite pictures and meteorological analysis of a developing low in the central United States, Mon. Wea. Rev. 89:429-445.
4. Leese, J. A. (1962) The role of advection in the formation of vortex cloud patterns, Tellus 12:409-421.
5. Hansen, J., and Thompson, A. H. (1964) Vertical motion calculations and satellite cloud observations over the western and central United States, J. Appl. Meteor. 4:18-30.
6. Nagle, R. E., Clark, J. R., and Holl, M. M. (1966) Tests of the diagnostic-cycle routine in the interpretation of layer-cloud evolutions, Mon. Wea. Rev. 94:55-66.
7. Barr, S., Lawrence, M. B., and Sanders, F. (1966) TIROS vortices and large scale vertical motion, Mon. Wea. Rev. 94:675-696.
8. Carlson, T. N. (1980) Airflow through midlatitude cyclones and the comma cloud pattern, Mon. Wea. Rev. 108:1498-1509.
9. Millard, J., and Carr, F. (1982) Composite study of comma clouds and their association with severe weather over the great plains, in Preprints of the 9th Conference on Weather Forecasting and Analysis (Seattle), American Meteorological Society, Boston, pp 402-406.
10. Carr, F. (1981) Personal communication.
11. Fuelberg, H. E. (1974) Reduction and Error Analysis of the AVE II Pilot Experiment Data, NASA Contract Report CR-120496, Marshall Space Flight Center, Alabama, 131 pp.

## References

12. Gerhard, M. L., Fuelberg, H. E., Williams, S. F., and Turner, R. E. (1979) AVE-SESAME I: 25-mb Sounding Data, NASA Tech. Memo. TM-78256, Marshall Space Flight Center, Alabama, 360 pp.
13. Sanders, F. (1981) Personal communication.
14. Moore, J., and Fuelberg, H. E. (1981) A synoptic analysis of the first AVE-SESAME '79 period, Bull. Am. Meteor. Soc. 62:1577-1590.
15. Jedlovec, G., and Fuelberg, H. E. (1981) A synoptic-scale kinematic energy analysis of the 10-11 April SESAME '79 period, in Proceedings of the SESAME 1979 Preliminary Results Workshop, Huntsville, Alabama, pp 21-23.
16. Cressman, G. P. (1959) An operational objective analysis system, Mon. Wea. Rev. 87:367-374.
17. Stephens, J. J., and Stitt, J. M. (1970) Optimum influence radii for interpolation with the method of successive corrections, Mon. Wea. Rev. 98:680-687.
18. Stephens, J. J. (1967) Filtering response of selected distance-dependent weight functions, Mon. Wea. Rev. 95:45-46.
19. Ridge, D. (1982) Diagnosis of the Comma Cloud of 10 April 1979, Masters' thesis, University of Oklahoma, Norman, Oklahoma, 108 pp. *AD A125254*
20. Bluestein, H. B. (1979) Quasigeostrophic Theory, unpublished, mimeograph class notes, 52 pp.
21. Krishnamurti, T. N. (1968) A study of a developing wave cyclone, Mon. Wea. Rev. 96:208-217.
22. O'Brien, J. J. (1969) Alternative solutions to the classical vertical velocity problem, J. Appl. Meteor. 9:197-203.
23. Wiin-Nielsen, A. (1959) On a graphical method for an approximate determination of the vertical velocity in the mid-troposphere, Tellus, 11:432-440.
24. Trenberth, K. E. (1977) On the interpretation of the diagnostic quasi-geostrophic omega equation, Mon. Wea. Rev. 106:131-137.
25. Orlandi, I. (1975) A rational subdivision of scales for atmospheric processes, Bull. Am. Meteor. Soc. 56:527-530.
26. Palmen, E., and Newton, C. W. (1969) Atmospheric Circulation Systems, Academic Press, New York, 603 pp.
27. Wilson, G. (1981) Structure and dynamics of important mesoscale systems influencing the thunderstorm development during April 10-11, 1979 (AVE SESAME I), in Proceedings of the SESAME 1979 Preliminary Results Workshop, Huntsville, Alabama, pp 28-31.
28. Alberty, R. L., Burgess, D. W., Hane, C. E., and Weaver, J. F. (1979) SESAME 1979 Operations Summary, National Oceanic and Atmospheric Administration, Boulder, Colorado, 253 pp.
29. Uccellini, L. W., and Johnson, D. R. (1979) The coupling of upper and lower tropospheric jet streaks and implications for the development of severe convective storms, Mon. Wea. Res. 107:682-703.
30. Benjamin, S. G., and Carlson, T. N. (1981) Numerical simulations of the severe storm environment for the 10-11 April 1979 (SESAME-I) case, in Preprints of the 12th Conference on Severe Local Storms (San Antonio), American Meteorological Society, Boston, pp 201-204.

## References

31. Kocin, P. J., Uccellini, L. W., and Petersen, R. A. (1981) The role of jet streak "coupling" in the development of the 10-11 April 1979 Wichita Falls tornado outbreak, in Preprints of the 12th Conference on Severe Local Storms (San Antonio), American Meteorological Society, Boston, pp 560-563.
32. Miller, R. C. (1975) Notes on Analysis and Severe-Storm Forecasting Procedures of the Air Force Global Weather Central, AWS TR 200 (Revised), Chapters 1, 4, and 11.

EN

FILM

9-83

DTIC